Full vehicle road testing of magnetorheological-based intelligent suspension for sport utility vehicles

OPEN ACCESS
IOP Publishing
Smart Materials and Structures
Smart Mater. Struct. **34** (2025) 085025 (25pp)
https://doi.org/10.1088/1361-665X/adf926

Full vehicle road testing of magnetorheological-based intelligent suspension for sport utility vehicles

Leng Dingxin[1], **Zhou Xu**[1], **Lyv Peng**[1], **Liu Guijie**[1] and **Li Yancheng**[2,*]

[1] Department of Mechanical and Electrical Engineering, Ocean University of China, Qingdao, Shandong, People's Republic of China
[2] School of Civil and Environmental Engineering, University of Technology Sydney, Ultimo, NSW 2007, Australia

E-mail: Yancheng.li@uts.edu.au

Received 21 April 2025, revised 2 July 2025
Accepted for publication 7 August 2025
Published 21 August 2025

Abstract

Vibration control in intelligent vehicle suspension utilizing magnetorheological (MR) dampers has attracted increasing attention. However, a practical real-time controller with easy implementation for sport utility vehicles (SUVs) and experimental validation have not been fully developed. To address this issue, the present study proposes a novel control algorithm for SUVs equipped with double-wishbone MR-based intelligent suspension. This algorithm directly calculates the desired current for the MR suspension based on vehicle sensor signals, eliminating the need for a complex inverse model of the MR damper and associated force tracking challenges. Firstly, the working principle of MR suspension systems is discussed, followed by experimental investigations of the dynamic behavior of a manufactured MR fluid damper. Next, a controller designed to balance comfort and attitude compensation for full-vehicle vibration suppression is proposed. Its control effectiveness for vertical comfortability is validated by a quarter SUV with a double-wishbone MR damper, and finally its effectiveness for vertical and attitude mitigation is evaluated through comprehensive practical road testing of an SUV across various road profiles. The results demonstrate significant reductions in the vehicle body acceleration and the pitch and roll angles when utilizing the proposed controller. This study provides a straightforward control algorithm for mitigating vertical motion and improving the dynamic responses of SUVs with MR-based intelligent suspension systems.

Keywords: magnetorheological suspension, combined vertical and attitude control, full-vehicle testing, SUV, road test

* Author to whom any correspondence should be addressed.

1. Introduction

Sport utility vehicles (SUVs) have gained popularity due to their versatility, allowing for both urban driving and off-road capability [1]. To balance off-road handling requirements and ride comfort, an intelligent suspension system is desired, whose damping should vary depending on the diverse and complex road conditions. One potential solution is to equip SUVs with intelligent damping suspension systems, whose damping coefficients can be tuned by semi-active or active controllers [2–4]. In recent decades, the magnetorheological (MR) damper has attracted great attention due to its controllable damping coefficients, fast-time response, easy implementation and fail-safe mode, and can be considered as a potential candidate for SUV intelligent suspension [5].

The vibration mitigation effectiveness of MR suspension was first evaluated using a quarter-car model. Li *et al* studied MR semi-active suspension for a quarter-car model by self-tuning an LQG controller, and its superiority to passive suspension was validated [6]; Hu *et al* developed semi-active MR suspension combined with negative-stiffness components for a quarter-car system, and an excellent vibration attenuation performance was derived comparable to that of active suspension [7]; Puneet *et al* designed a cost-effective MR suspension on a quarter-car model, and a sensor-based controller was proposed for vehicular vibration mitigation [8]; Kumar and Bhushan conducted a dynamic analysis of a quarter-car model with MR suspension, and the numerical results verified the reduction in settling time, peak displacement and root mean square (RMS) acceleration [9]. In addition, studies on MR intelligent suspension for the half-car model were conducted [10, 11]. These studies proved that the vertical acceleration of a quarter-car or half-car with MR intelligent suspension was reduced. However, the above-mentioned models generally utilized simplified dynamic systems, in which a sprung mass represented as rigid blocks was connected directly to coil springs and dampers, overlooking the practical suspension frame structures and mechanical connections. That is, by simplified laboratory tests, the effectiveness of MR-based suspension on realistic quarter-car or half-car vehicle dynamics cannot be explored.

Beyond the aforementioned quarter-car and half-car models, investigations into MR intelligent suspension for full vehicles have been conducted. Xie *et al* performed a simulation study on full-vehicle MR intelligent suspension using a visual view controller, and showed that the mean square values of sprung mass acceleration were reduced by 82% compared to the passive suspension values [12]; Zareh *et al* experimentally studied laboratory prototyped MR suspension for a light commercial vehicle, which proved its effectiveness for passenger comfort [13]; Krauze *et al* performed an experiment for a commercial all-terrain vehicle equipped with MR intelligent suspension, and the results showed the acceleration in vehicle body was attenuated [14]. The current investigations imply the vibration suppression of a full vehicle with MR suspension. However, in testing, research is mainly focused on full vehicles under specific road profiles (e.g. predominantly bumps and harmonic excitation), in which the primary focus is the evaluation of ride comfortability using the index of the vehicle body's vertical acceleration. Few studies have been conducted on SUV full-vehicle testing under complex road profiles, in which the vehicle body's vertical acceleration and vehicle attitude angle are simultaneously expected to be controlled. That is, the vibration mitigation effectiveness of comprehensive testing of a SUV with MR suspension across multiple road excitations is not fully verified.

In the above-mentioned studies on vehicles with MR suspension, control algorithms play a crucial role in enhancing vehicle stability and passenger comfort. Currently, two main categories of control algorithms have been proposed: model-based control and model-free control. Model-based control requires detailed information about the vehicle's dynamic modal characteristics, such as its mass and stiffness matrices, as well as an accurate inverse model of the MR dampers to generate precise control outputs based on feedback signals. Examples of model-based control methods on MR suspension include sliding mode control [11], linear quadratic regulator control [15] and $H\infty$ control [16]. However, in reality, constructing a precise dynamic vehicle model is complex, and its key modal parameters may degrade over time, leading to a downgrade in performance. In addition, developing an inverse model for MR dampers is a tedious process that demands extensive experimental data [17, 18]. In contrast, model-free control does not require predefined information and operates based on an understanding of the vehicle dynamics and control mechanisms. These algorithms, such as adaptive control [19–21] and fuzzy logic control [22–24], generate control outputs by evaluating vehicle response magnitudes, such as the acceleration of the sprung and unsprung masses, and are robust against external disturbances caused by varying road profiles. However, in current model-free controllers, the reliance on expert knowledge and initial tuning parameters, combined with an inability to handle highly dynamic environments, creates challenges in applications. Therefore, our aim is to develop a practical and feasible control algorithm for MR suspension for engineering applications.

In this study, an intelligent MR suspension is proposed for SUV vibration mitigation, and its effectiveness is validated by realistic road testing. A practical controller is developed for full-vehicle all-state vibration mitigation, whose key feature is the ability to directly derive the desired current for the MR intelligent suspension, eliminating the need for real-vehicle precise dynamic modal information and avoiding the complexities associated with inverse modeling of MR dampers. The main contributions of this work are summarized as follows:

(1) A feasible model-free control algorithm for SUV vehicles with MR suspension is designed for practical applications, in which the vertical vibration of the vehicle body and the attitude state of the full-vehicle angle are simultaneously suppressed.

(2) We experimentally investigate a practical quarter-SUV prototype model with double-wishbone MR suspension.
(3) Realistic testing of MR suspension assembled in an SUV full vehicle is conducted, and the vibration mitigation effectiveness is fully validated under various road profiles.

The remainder of this paper is organized as follows: section 2 outlines the working principles of semi-active MR intelligent suspension systems and presents experimental studies on the dynamic behavior of a manufactured MR fluid (MRF) damper. The proposed controller for balanced comfortability and attitude state is introduced in section 3 and its design principle is explained in detail. To validate the comfortability control effectiveness of the proposed controller, section 4 investigates a quarter-vehicle model with semi-active MR suspension, which serves as a 1:1 prototype of full SUV suspension. Section 5 examines both vertical and attitude vibration mitigation in a full realistic SUV equipped with double-wishbone MR intelligent suspension under various road profiles. Finally, the main conclusions of this research are summarized in section 6.

2. MR intelligent suspension

2.1. Working principle

The conceptual control framework of vehicle intelligent suspension with an MRF damper is shown in figure 1. Four MRF dampers are developed for vehicle suspension; that is, two dampers at the front and two at the rear. By regarding the required damping force of the vehicle, the key design parameters of MRF dampers are determined. As shown in figure 1, when a vehicle is under external excitation, its dynamic responses (e.g. vertical acceleration, pitch angle and roll angle) are measured by multiple sensors; the sensor signals are input into a pre-designed controller explained in section 3.1, by which the desired current to the MRF damper is determined for vibration mitigation.

2.2. MR damper and modeling

The damping coefficient of the original passive damper is 1800 Ns m^{-1} for the studied classical middle-weight vehicle in section 5.1. Referred to in the work of Choi and Sung [25], the optimal damping coefficient of an MRF damper for the adopted full-vehicle model is determined by the transmissibility index, which is the ratio between the amplitude of the road excitation and the sprung mass. For the designed MRF damper, the damping coefficient at zero field is 1200 N s m^{-1}, and the maximum damping is 2700 N s m^{-1} by applying a current of 3 A. The manufactured damper, produced by Shenzhen Upward Tech, is shown in figure 2. The damper has a single-tube structure, which consists of a chamber with a piston and the MRF. When the piston moves in the axial direction, the MRF moves in the chamber. Along the MRF flow direction, a magnetic field is applied and the field strength is controlled by the current signal. As the damping value of the MRF changes, the damping force is adjusted.

To evaluate the dynamic behavior of the MRF damper, a series of experimental tests are conducted. The experimental setup is shown in figure 3.

As shown in figure 3, an electromagnetic exciter is utilized to supply a harmonic excitation signal. One end of the MR damper is fixed and the other end is mounted on the electromagnetic exciter, which causes the MR damper to move with the excited displacement signal. A force sensor is fixed between the MR damper and the electromagnetic exciter to measure the force signal generated by the damper. The magnetic coil is energized by adjusting the DC power, which provides a DC current from 0.0 A to 3.0 A at intervals of 1.0 A. A data acquisition device is utilized to record the excitation and the response signals and then transferred to a computer for processing and analyzing. The force–displacement curves of the MR damper under sinusoidal loading with frequencies of 4.0 and 5.5 Hz and a displacement amplitude of 30.0 mm are shown in figures 4 and 5.

MRF has obvious nonlinear hysteresis characteristics, and linear viscoelastic parameter models cannot simulate the parallelogram characteristics of MRF hysteresis loops. As a classic model for describing hysteresis loops, the Bouc–Wen model can simulate this characteristic well, especially under large strain amplitudes. To establish the relationship between the input current and the output force of the MRF damper, a nonlinear Bouc–Wen model is established [12]:

$$\begin{cases} F = c\dot{x} + kx + \alpha z \\ \dot{z} = -\gamma |\dot{x}| z |z|^{n-1} - \zeta \dot{x} |z|^{n} + A\dot{x} \end{cases} \tag{1}$$

where c is the viscosity coefficient of the MR material after yielding; $\dot{x}$ is the relative velocity of the damper piston; z is the hysteresis displacement; γ is the hysteresis width related parameter; ζ is the hysteresis height related parameter; α is the proportional adjustment coefficient between the hysteresis force and the output force; and A is the proportional coefficient related to the maximum output force.

In the process of parameter identification using experimental data, c and k were found to have an approximately linear relationship with the input current. The model parameters are linearly approximated with the input current as follows:

$$c = c_1 I + c_0 \tag{2}$$

$$k = k_1 I + k_0. \tag{3}$$

Parameter optimization is conducted to determine the above coefficients based on the experimental data. The identified parameters are listed in table 1.

The force–displacement and force–velocity hysteresis loops between the model and testing curves are compared using sinusoidal loading with an amplitude of 30.0 mm and different frequencies (e.g. 4.0 Hz and 5.5 Hz), as shown in figure 6.

The mean absolute percentage error (MAPE) index, shown in equation (2–1), is utilized to evaluate the fitting accuracy of the dynamic model for the MR damper:

$$\mathrm{MAPE} = \frac{100\%}{n} \sum_{n}^{i=1} \left| \frac{\hat{y}_i - y_i}{y_i} \right|. \tag{2-1}$$

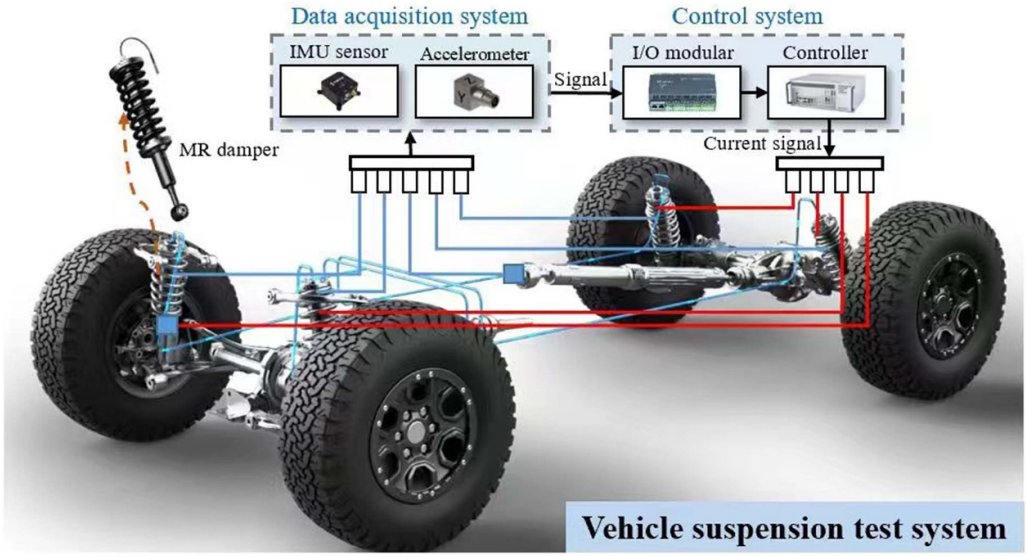

Figure 1. Conceptual control framework of vehicle intelligent suspension with MRF damper.

Figure 2. The manufactured MRF damper.

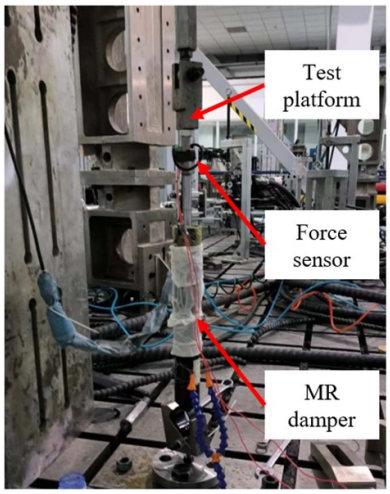

Figure 3. Experimental setup for measuring dynamic properties of MR damper.

Here, $\hat{y}_i$ and y_i denote the model and experimental data, respectively. It is known that the smaller MAPE is, the better the accuracy. The MAPE values are listed in table 2.

It is demonstrated in figure 6 and table 6 that the Bouc–Wen model not only describes the relationship between force and displacement well, but also portrays the nonlinear curve between force and velocity. That is, the effectiveness of the dynamic model is proved.

3. Controller for MR-based intelligent suspension

3.1. Control principle

Here, a control algorithm for full-vehicle balanced comfort and attitude compensation is designed. The feedback signals include four sprung mass accelerations collected on top of the dampers, four unsprung mass accelerations at the lower end of the dampers near the tires, and vehicle attitude signals from an inertial measurement unit (IMU). These IMU signals consist of the pitch angle, roll angle and vertical acceleration of the vehicle mass center. The control framework generates four control outputs to drive the MR dampers for appropriate reactions. The proposed controller considers both vertical vibration control and body attitude control, including full-vehicle pitch and roll. The detailed control framework is presented in figure 7.

From the framework in figure 7, a sky-hook control algorithm is utilized to control the vertical vibration of individual dampers, and the desired current is calculated as I_1; an attitude compensation controller is designed to suppress the vehicle body pitch and roll motions, and the corresponding desired current of each suspension is derived as I_2; then, a mixed logic rule is developed by combining I_1 and I_2, by which the final current I_{desire} is determined.

In the proposed controller, the vehicle body center acceleration responses (e.g. vertical acceleration, pitch angular acceleration and roll angular acceleration) are monitored in real time. The measured accelerations at the two ends of the dampers can be integrated to obtain the velocity, such as the relative velocity of each damper. Considering the frequency of road excitation, a low-pass filter is utilized to remove high-frequency noise in the acceleration signals. The sprung mass velocity of each individual suspension can be obtained by considering the geometrical layout. Similarly, the unsprung mass velocity is also derived. Additionally, the velocity of the damper, or the relative velocity between the sprung mass and

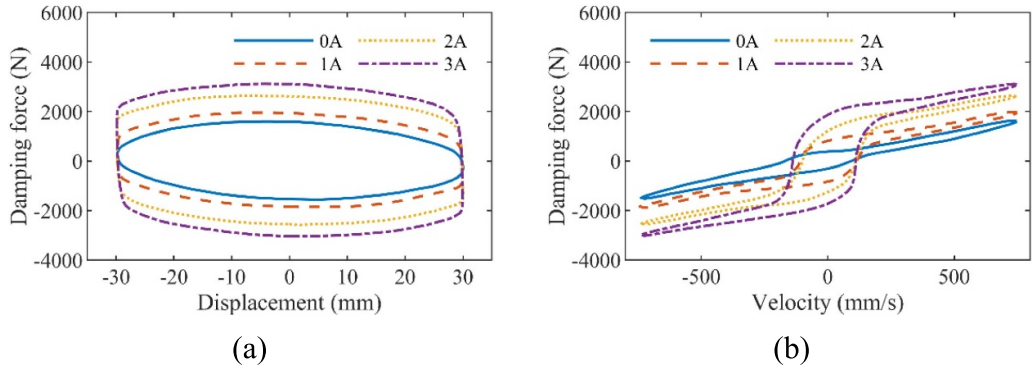

Figure 4. Experimental dynamic behaviors of MRF damper (displacement amplitude 30.0 mm, 4.0 Hz): (a) force–displacement curve, (b) force–velocity curve.

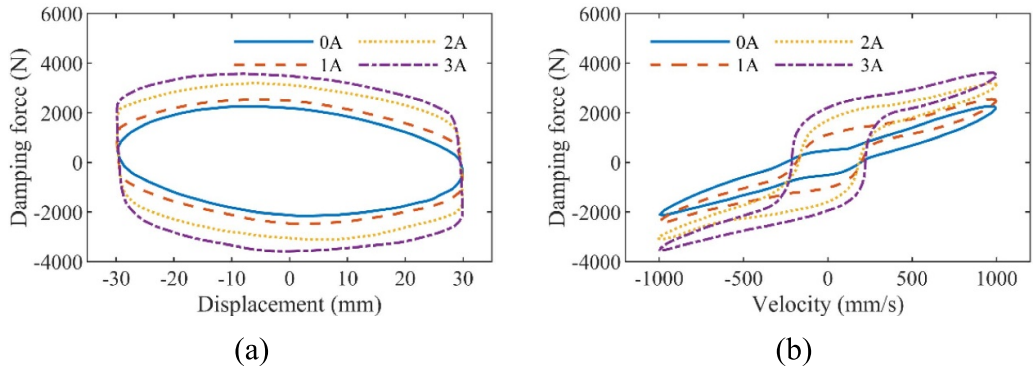

Figure 5. Experimental dynamic behaviors of MRF damper (displacement amplitude 30.0 mm, 5.5 Hz): (a) force–displacement curve, (b) force–velocity curve.

Table 1. Key parameters of the hyperbolic tangent model.

Symbols	c_0	c_1	k_0	k_1	α	γ	ζ	A
Values	2019.6	329.5	1876.1	962.1	1327.9	950.9	−175.7	−1187.3

unsprung mass, is critical since it not only defines the damping force but also provides critical information on whether the damper is in compression or rebounding.

3.2. Vertical control

For an individual suspension, a practical sky-hook algorithm is applied for vertical comfortability, as shown in figure 8.

As denoted in figure 8, m_s and m_u are the sprung and unsprung mass, respectively; z_s, z_u and z_r denote the vertical displacements of the sprung and unsprung mass, and road excitation, respectively; k_s and k_t are the stiffness of suspension and unsprung mass. The sky-hook controller is expressed as

$$I_{in} = \begin{cases} I_{max}, & \dot{z}_s \cdot (\dot{z}_s - \dot{z}_u) \geqslant 0 \\ I_{min}, & \dot{z}_s \cdot (\dot{z}_s - \dot{z}_u) < 0. \end{cases} \tag{4}$$

The above controller is used to control the vertical motions between the four wheels and the chassis. Since each wheel is subjected to random road excitation, the vehicle body may exhibit pitch and roll at the same time, and these three motions affect each other. To ensure the riding comfort, an attitude controller should be designed for full-vehicle state compensation.

3.3. Attitude compensation

The main objective of attitude control is to regulate and maintain the orientation of the vehicle body according to the desired attitude profile. This involves controlling the vehicle's rotational motions, such as pitch and roll, to achieve vehicle stability and efficient maneuvering. In particular, the developed controller should secure the vehicle's response to disturbances caused by the sudden changes in road profile, driver operation, etc.

Here, the vehicle's rotational signals, such as the pitch and roll angles and damper status, are used as feedback signals. Undesirable vehicle pitch or roll angles serve as a trigger threshold to activate the attitude control, which is combined with the damper status to determine the exact control command to regulate the vehicle orientation.

For each damper, it is critical to underpin its current status, e.g. whether it is under compression or restoration compared

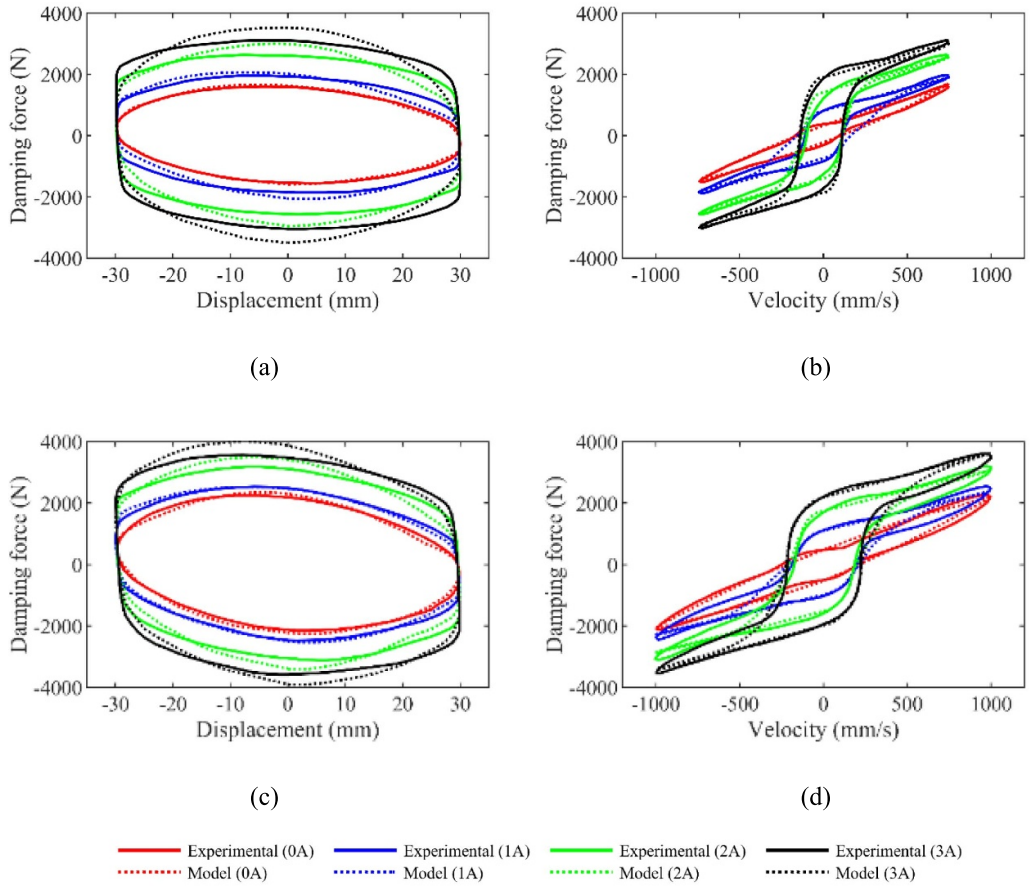

Figure 6. Comparison of hysteresis loops between dynamic model and experimental data under harmonic loading: (a) force–displacement curve (4.0 Hz), (b) force–velocity curve (4.0 Hz), (c) force–displacement curve (5.5 Hz), (d) force–velocity curve (5.5 Hz).

Table 2. MAPE values for modeling and experimental data of MR damper.

Current (A)	Force–displacement curve (4.0 Hz–30 mm)	Force–velocity curve (4.0 Hz–30 mm)	Force–displacement curve (5.5 Hz–30 mm)	Force–velocity curve (5.5 Hz–30 mm)
0.0	0.1376	0.1274	0.0962	0.1914
1.0	0.4326	0.3308	0.0967	0.3695
2.0	0.1855	0.2298	0.1745	0.3528
3.0	0.2156	0.1543	0.1480	0.3259

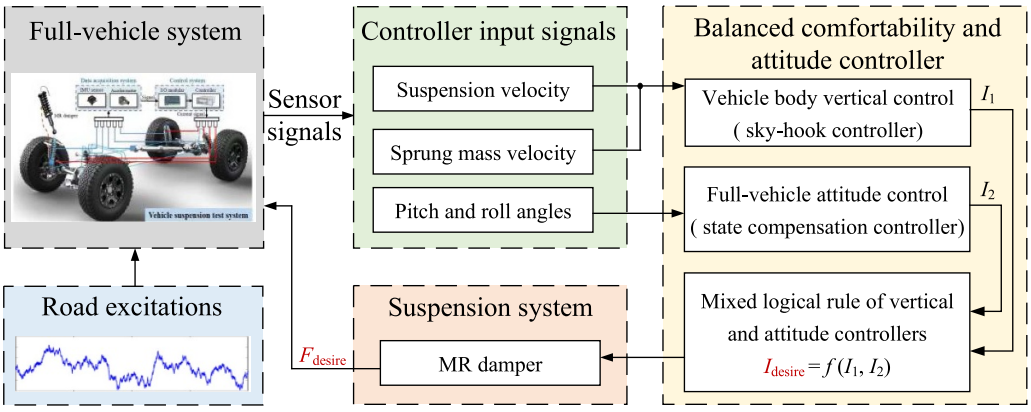

Figure 7. Control framework of full vehicle with MR suspension.

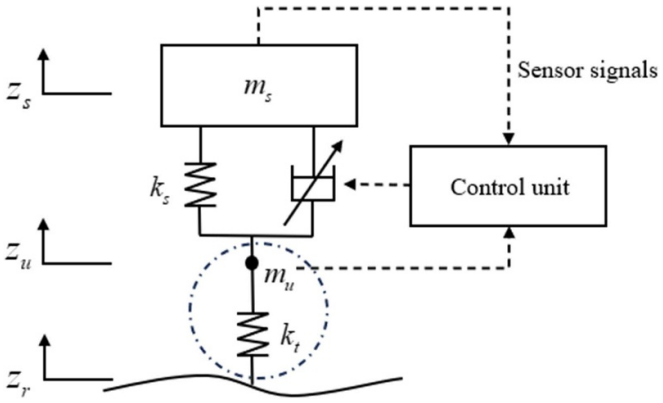

Figure 8. Practical sky-hook controller for quarter suspension.

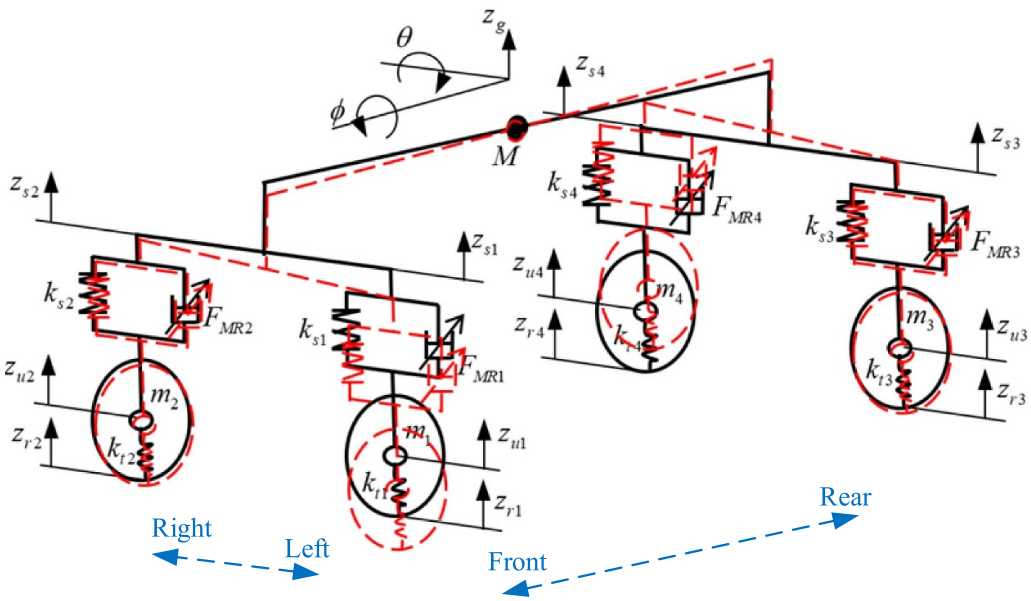

Figure 9. Full vehicle model with MR suspensions ($\theta < 0, \phi < 0$).

to its original undeformed stroke. In addition, the damper velocity is required to determine whether it approaches or moves away from its original state, which can be used to predict its contribution toward its future position; thirdly, a current signal is then confirmed to minimize or eliminate the vehicle body angle motion. A detailed illustration using the left front wheel is explained as follows:

Assuming the pitch and roll angles are negative (e.g. $\theta < 0, \phi < 0$), the vehicle motion is shown by the red dashed line in figure 9.

Taking the left front wheel as an example, with the vehicle angle motion in figure 8, the left front suspension is in compression. Then, the relative velocity of the real-time suspension can be calculated by $\dot{z}_{\mathrm{ui}}$ and $\dot{z}_{\mathrm{si}}$, and its motion tendency can be predicted. That is, if the direction of suspension relative velocity is downward, the suspension keeps compression, and the maximum current should be applied to attenuate the compression, which is beneficial to compensate the vehicle body's angle motion and vice versa (e.g. zero current is applied). Consequently, the controller for the MRF damper in the left front suspension can be expressed as

$$\theta < 0, \phi < 0 \begin{cases} v_{12-\mathrm{LF}} < 0, I = I_{\max} \\ v_{12-\mathrm{LF}} \geqslant 0, I = 0. \end{cases} \tag{5}$$

in which $v_{12-\mathrm{LF}}$ is the suspension relative velocity and I is the desired current. Similarly, when the pitch angle and the roll angle are positive (e.g. $\theta > 0, \phi > 0$), the angle controller for the MRF damper in the left front suspension can be expressed as

$$\theta \geqslant 0, \phi \geqslant 0 \begin{cases} v_{12-\mathrm{LF}} < 0, I = 0 \\ v_{12-\mathrm{LF}} \geqslant 0, I = I_{\max} \end{cases} \tag{6}$$

In addition, if the pitch and roll angles are of opposite sign (e.g. $\theta \cdot \phi < 0$), the suspension states (e.g. compression or rebounding state) cannot be directly identified. The angle-induced arc length is calculated and compared to evaluate the present suspension state; then, according to the potential compression or tension state determined by the suspension velocity, the desired current for the MR damper is derived. The

detailed angle controller for the MRF damper in the left front suspension is designed as

$$\theta<0,\phi\geqslant 0\begin{cases}|l_{\mathrm{f}}\cdot\theta|\geqslant\left|\frac{b_{\mathrm{f}}}{2}\cdot\phi\right|\begin{cases}v_{12-\mathrm{LF}}<0, I=I_{\max}\\ v_{12-\mathrm{LF}}\geqslant 0, I=0\end{cases}\\ |l_{\mathrm{f}}\cdot\theta|<\left|\frac{b_{\mathrm{f}}}{2}\cdot\phi\right|\begin{cases}v_{12-\mathrm{LF}}>0, I=0\\ v_{12-\mathrm{LF}}\ 0, I=I_{\max}\end{cases}\end{cases}\tag{7}$$

$$\theta\geqslant 0,\phi<0\begin{cases}|l_{\mathrm{f}}\cdot\theta|\geqslant\left|\frac{b_{\mathrm{f}}}{2}\cdot\phi\right|\begin{cases}v_{12-\mathrm{LF}}<0, I=0\\ v_{12-\mathrm{LF}}\geqslant 0, I=I_{\max}\end{cases}\\ |l_{\mathrm{f}}\cdot\theta|<\left|\frac{b_{\mathrm{f}}}{2}\cdot\phi\right|\begin{cases}v_{12-\mathrm{LF}}<0, I=I_{\max}\\ v_{12-\mathrm{LF}}\geqslant 0, I=0.\end{cases}\end{cases}\tag{8}$$

The attitude control strategies of the other three sets of dampers vary due to its geometric location. For example, under pitch motion when the front dampers are in compression, the rear dampers would be in restoration. However, they can be determined by following the same principle, e.g. maintaining or forcing the dampers to move back to the original location.

3.4. Mixed rule of vertical and attitude controller

By comprehensively considering the vertical and attitude controllers in sections 3.2 and 3.3, the combining logical rule is defined as follows:

(1) If the desired applied currents of the vertical controller and state controller are all $I_{\max}$, then the desired current is $I_{\max}$;
(2) If the desired applied currents of the vertical controller and state controller are all $I_{\min}$, then the desired current is $I_{\min}$;
(3) If the desired applied currents of the vertical controller and state controller are $I_{\max}$ and $I_{\min}$, then the desired current is $I=\rho I_{\max}, 0\leqslant\rho\leqslant 1$;
(4) If the desired applied currents of the vertical controller and state controller are $I_{\min}$ and $I_{\max}$, then the desired current is $I=\mu I_{\max}, 0\leqslant\mu\leqslant 1$.

Here, $I_{\max}$ and $I_{\min}$ are respectively the maximum and minimum applied current of the MRF damper, e.g. 3.0 A and 0.0 A; the regulating parameters, ρ and μ, are determined by extensive trials of full-vehicle numerical simulations for the best mitigation performance. The detailed full-vehicle dynamic model is presented in appendix A. In the present work, ρ and μ are adopted respectively as 0.70 and 0.10, and the detailed analysis is shown in appendix C. It should be noted that these two parameters can also be determined by real-vehicle testing; however, numerous experimental costs should be considered.

4. Realistic quarter-car model with double-wishbone MR intelligent suspension

To validate the effectiveness of the proposed controller for vertical comfortability, a commercial quarter-SUV double-wishbone MR suspension model is constructed. The mathematical model is established and an experimental platform is developed for a 1:1 scale prototype. Control evaluations are investigated.

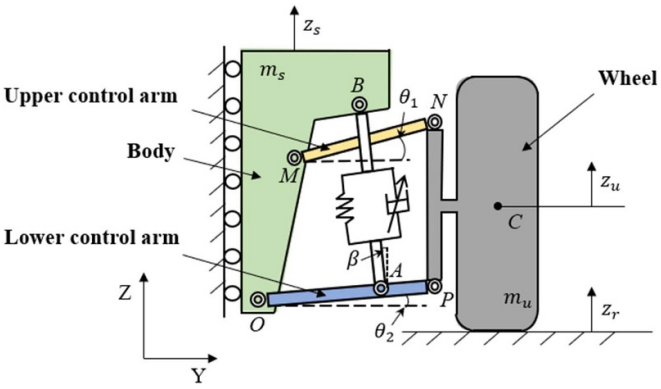

Figure 10. A quarter double-wishbone-type suspension model.

4.1. Mathematical model

Figure 10 shows a quarter-SUV double-wishbone model with an MRF damper, showing the sprung mass, unsprung mass, MRF damper and spring stiffness. The sprung mass (m_{s}) is assumed to be a rigid suspension body and the unsprung mass (m_{u}) comprises the wheel system. The stiffness of the suspension coil spring (k_{s}) is assumed to be a linear element within the working deformation range. The suspension damping is tunable by an MRF damper. It is noted that the coordinate origin (point O) is set as the connection point between the bottom wishbone and sprung mass. Here, the vertical and horizontal directions are the Z and Y axis, respectively.

A numerical model of quarter double-wishbone-type MRF suspension is established in the geometrical and force analysis. Some assumptions are made as follows:

(1) The sprung mass (suspension body) only moves in the vertical direction, while the unsprung mass (tire system) can move in the vertical and translation directions with potential free rotation;
(2) The wishbone is considered as a rigid body and its mass is ignored;
(3) Friction is not considered in the hinge connection of the quarter-vehicle model.

By conducting a geometrical and force analysis (appendix B), the dynamic equation of the quarter double-wishbone MR suspension model is derived:

$$\begin{cases}m_{\mathrm{s}}\ddot{z}_{\mathrm{s}}=\lambda F_{\mathrm{d}}\\ m_{\mathrm{u}}\ddot{z}_{\mathrm{u}}=-\lambda F_{\mathrm{d}}+k_{\mathrm{t}}\left(z_{\mathrm{r}}-z_{\mathrm{u}}\right)\end{cases}.\tag{9}$$

in which m_{s} and m_{u} represent the mass of the vehicle body and wheel, respectively; $z_{\mathrm{s}}, z_{\mathrm{u}}$ and z_{r} are the vertical displacement of the sprung mass, unsprung mass and road excitation; k_{s} and k_{t} denote the stiffness of the suspension and unsprung mass; and λ is a geometry parameter related to the suspension structure.

The corresponding state space equation of equation (10) can be written as

$$\begin{cases} \dot{X} = AX + BU \\ Y = CX + DU \end{cases} \tag{10}$$

where X is a state variable as $X = \begin{bmatrix} z_u & z_s & \dot{z}_u & \dot{z}_s \end{bmatrix}^T$; the input variables ($U$) include the road excitation and control force of the MRF damper (F), $U = \begin{bmatrix} z_r & F \end{bmatrix}^T$; and system matrix A, B, C and D are shown as follows:

$$A = \begin{bmatrix} 0 & 0 & 1 & 0 \\ 0 & 0 & 0 & 1 \\ -\frac{\lambda k_s}{m_u \cos\beta} - \frac{k_t}{m_u} & \frac{\lambda k_s}{m_u \cos\beta} & 0 & 0 \\ \frac{\lambda k_s}{m_s \cos\beta} & -\frac{\lambda k_s}{m_s \cos\beta} & 0 & 0 \end{bmatrix},$$

$$B = \begin{bmatrix} 0 & 0 \\ 0 & 0 \\ \frac{k_t}{m_u} & \frac{\lambda}{m_u \cos\beta} \\ 0 & -\frac{\lambda}{m_s \cos\beta} \end{bmatrix},$$

$$C = E_{(4\times4)}, D = O_{(4\times2)},$$

in which $E_{(4\times4)}$ is an identity matrix and $O_{(4\times2)}$ is a zero matrix; β is the MRF damper dip angle. Here, the sprung and unsprung mass are set as 510.6 kg and 173.2 kg; the sprung and unsprung stiffness are 278 kN m^{-1} and 110 kN m^{-1}.

4.2. Road excitations

The random road profile (z_r) is generated using the power spectrum density (PSD), as outlined by ISO 8608: 2016:

$$G_d(n) = G_d(n_0)\left(\frac{n}{n_0}\right)^{-w}. \tag{11}$$

in which n represents the spatial frequency in units of m^{-1}; n_0 represents the reference spatial frequency, $n_0 = 0.01$ m^{-1}; G_q (n_0) represents the road roughness coefficient in units of m^3; w represents the frequency index, usually taken as $w = 2$.

Using the filter white-noise method, the road profile is expressed as

$$\dot{z}_r(t) = -2\pi n_1 v \cdot z_r(t) + 2\pi n_0 \sqrt{G_d(n_0) v} \cdot \omega(t). \tag{12}$$

in which z_r (t) represents the road excitation signal and ω (t) represents the unit white noise excitation signal. In this paper, a B-level road profile with a driving velocity of 20 km h^{-1} is produced for quarter MR suspension, as shown in figure 11.

4.3. Experimental testing

To evaluate the vibration control effectiveness of the proposed vertical control, a testing platform of quarter double-wishbone-type suspension is developed, as shown in figure 12, including modified MR suspension, an excitation system, multiple sensors and a real-time control system.

In the testing platform, the modified MR suspension prototype consists of a vehicle body representing a lumped mass, a tire system representing the unsprung mass, an MRF damper and a coil spring. A slide is utilized to guide the vertical motion of the sprung mass. The excitation system includes a vibration table, an industrial computer and a power control system, by which different excitations (e.g. harmonic loading, impulse and random road profile) can be input and produced. Two accelerometers (type: MEMS, ±50 g) are mounted, as shown in figure 13, to measure the acceleration of the sprung mass (the same as the top of the MR damper) and the bottom wishbone strut.

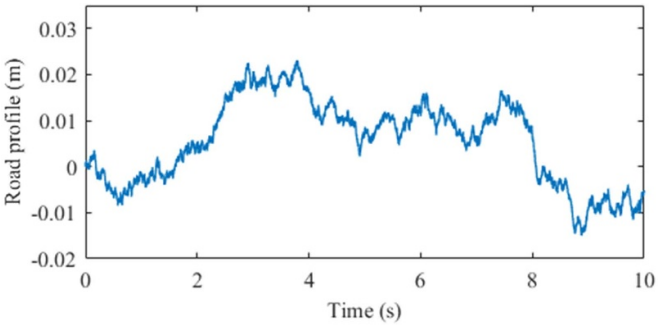

Figure 11. B-level road profile with driving velocity of 20 km h^{-1}.

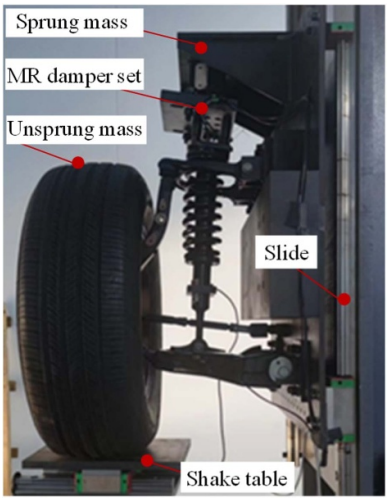

Figure 12. Testing platform of quarter-car model with double-wishbone strut.

4.4. Results and discussions

For a B-level road profile with a driving velocity of 20 km h^{-1}, the numerical and experimental results of MR suspension responses with the sky-hook controller are illustrated in figures 14 and 15, respectively. To further demonstrate the control effectiveness, the input variation and corresponding damping force variation are also presented in figure 16. Detailed responses in RMS values are listed in tables 3 and 4, in which positive values of the reduction ratio denote an improved performance and negative ones represent a downgraded performance.

Figure 13. Applied location of multiple sensors: (a) acceleration sensor (#1), (b) acceleration sensor (#2), (c) wire-type displacement sensor.

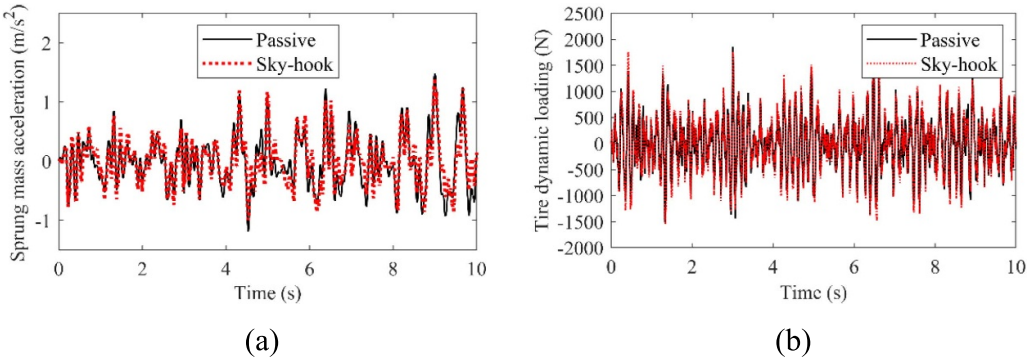

Figure 14. Numerical results of MR suspension (*B*-level road profile with driving velocity of 20 km h^{-1}): (a) sprung mass acceleration, (b) tire dynamic loading.

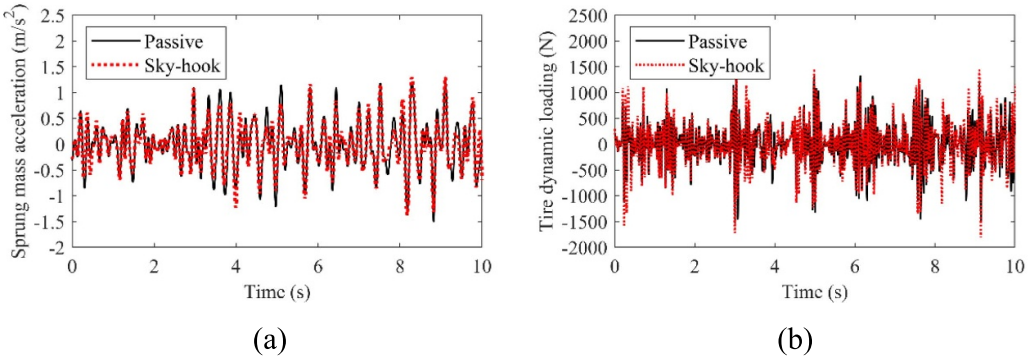

Figure 15. Experimental results of MR suspension (*B*-level road profile with driving velocity of 20 km h^{-1}): (a) sprung mass acceleration, (b) tire dynamic loading.

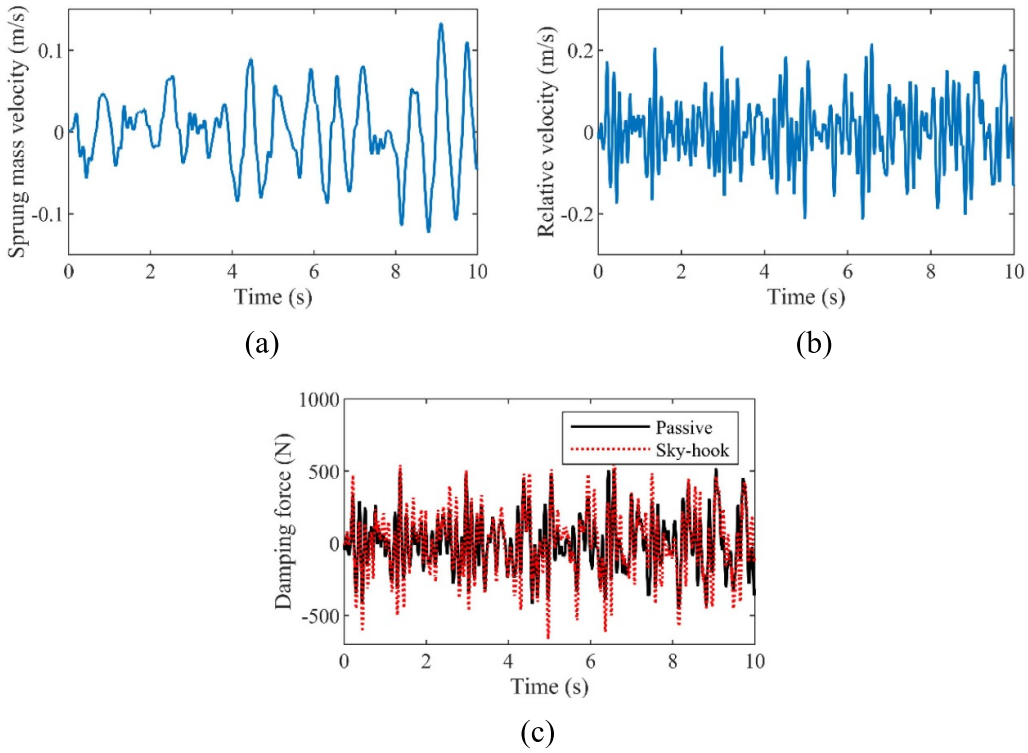

Figure 16. Controller information of quarter-SUV model with double-wishbone MR suspension (*B*-level road profile with driving velocity of 20 km h^{-1}): (a) input control signal: sprung mass velocity, (b) input control signal: relative velocity, (c) control damping force.

Table 3. RMS values of numerical results.

		Classical controllers	Reduction ratio
Index	Passive	Sky-hook	Sky-hook
Sprung mass acceleration (m s^{-2})	0.4433	0.3911	11.78%
Suspension dynamic displacement (m)	0.0039	0.0036	7.69%
Tire dynamic loading (N)	493.7	535.1	−8.39%

Note: Reduction ratio = (passive-semi-active)/passive × 100%.

Table 4. RMS values of experimental results.

		Classical controllers	Reduction ratio
Index	Passive	Sky-hook	Sky-hook
Sprung mass acceleration (m s^{-2})	0.4751	0.4396	7.47%
Tire dynamic loading (N)	402.2	421.2	−4.72%

Note: Reduction ratio = (passive-semi-active)/passive × 100%.

As shown, compared with passive suspension, sprung mass acceleration is reduced by the sky-hook controller, whose RMS values are respectively decreased by 11.78% and 7.47% in the numerical and experimental models. This finding validates the effectiveness of the vertical mitigation by the sky-hook controller. The proposed semi-active controller for balanced vertical and attitude compensation of a full SUV is further experimentally investigated in the following section.

5. Road testing of full vehicle with MR intelligent suspension

5.1. Testing vehicle and real-time control system

To validate the vibration control performance, full vehicle testing on an SUV is conducted, in which four MRF dampers replace the passive ones to form MRF suspension. The testing vehicle has double-wishbone struts in both the front and

Figure 17. Instrumentation of full-vehicle MR suspension system.

rear suspension. Eight accelerometers and one IMU are used to measure the dynamic responses of the sprung mass and unsprung mass, as shown in figure 17. The IMU is applied on the centroid of the vehicle body, and records the vertical acceleration and pitch and roll angles. The eight accelerometers are of capacitive type (range: ± 10 g, frequency-response range: 0–1300 Hz, sensitivity: 200 mV g^{-1}), and measure the acceleration of the sprung mass and unsprung mass at the ends of the MR dampers. The sensor data were processed by a low-pass filter with a cutoff frequency of 100 Hz, and the sampling frequency was set to 400 Hz. Additionally, a rapid prototype controller (type: Speedgoat, maximum sampling frequency: 200 kSPS, resolution ratio: 16 bits) was utilized to convert the proposed control algorithm in Simulink Real-Time into hardware control with the assistance of amplifiers. Electricity for the sensors, prototype controller and data acquisition system was provided by the vehicle power supply.

5.2. Testing roads

Tests are conducted using various road profiles at different vehicle speeds to simulate the different vibration modes. The testing profiles include sinusoidal waves, modified torture tracks with square pits, impact bump tracks, washboard pavements and Belgian blocks, as shown in figure 18. The use of different road profiles aims to excite the different vibration modal characteristics of the SUV full vehicle, as listed in table 5. These road profiles are inspired by the internal test standards of automotive manufacturers, such as Ford, GM and Toyota.

As shown in figures 16(a) and (b), the sinusoidal road is divided into two types: same-direction sinusoidal road and opposite-direction sinusoidal road. For the same-direction sinusoidal road, the road profile on both sides is identical, which mainly excites the vehicle's vertical motion given that the distance between the peaks is similar to that between the front and rear tires. With the opposite-direction sinusoidal road, the distance between adjacent peaks on the same side is equal to the vehicle wheelbase, while the profile difference on both sides of the road surface is equal to half of the vehicle wheelbase; hence, the roll motion is primarily excited. On the torture track with square pits (figure 16(c)), two identical square pits on both sides are followed by alternating square pits on each side; hence, vertical acceleration mitigation is firstly tested, followed by pitch and roll control. As shown in figure 16(d), on the impact bump track, identical bumps are presented, and control of the vehicle body's vertical and pitch angle is primarily evaluated. In figure 16(e), the random excitation pavement is a combination of Belgian block and cobblestone track, which excites all three vibration modes of the vehicle body (e.g. vertical displacement, pitch and roll motion) with varied frequency range.

It should be noted that, in each selected road profile, multiple trials were conducted to ensure repeatability of the test results. Additionally, to guarantee the corresponding mode excited, each realistic road profile of the commercial SUV is performed with a specific driving speed, as listed in table 5.

5.3. Full-vehicle testing results and discussions

The dynamic responses of a full-vehicle system under different road profiles are experimentally investigated. The vibration mitigation effectiveness of the proposed combined controller is compared with a classical sky-hook controller and passive suspension without MRF damper.

5.3.1. Sinusoidal road. Figures 19 and 20 respectively show the dynamic responses of the vehicle body in the time and frequency domains for a same-direction sinusoidal road and an opposite-direction sinusoidal road. The detailed RMS and peak values of vertical acceleration and roll angle are listed in tables 6 and 7. The reduction ratio is calculated as

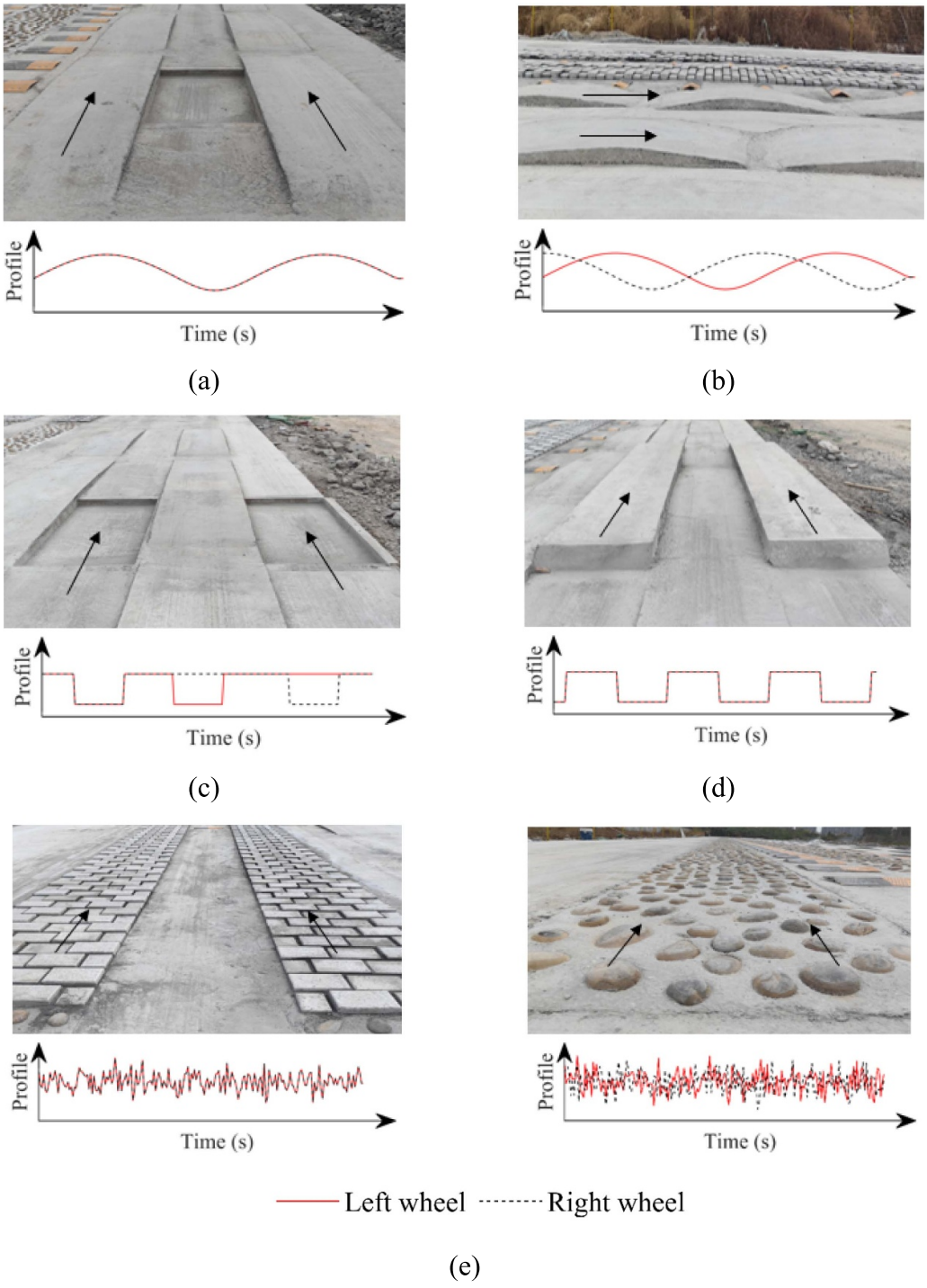

Figure 18. Testing road profiles: (a) same-direction sinusoidal road, (b) opposite-direction sinusoidal road, (c) torture track with square pits, (d) impact bump track, (e) random excitation (left: Belgian block, right: cobblestone).

$$\Gamma = \frac{p_0 - p_n}{p_0} \times 100\% \tag{13}$$

in which $n = 1, 2$ denoting semi-active suspension with the sky-hook controller and proposed controller, respectively; p_n is the performance indicator of the semi-active suspension system, namely the RMS and peak values of vertical acceleration, roll and pitch angle; p_0 is the corresponding performance indicator of passive suspension.

As shown in figures 19 and 20, compared with passive suspension, semi-active suspension with an MRF damper enhances the mitigation of the roll angle and vertical acceleration of the full-vehicle system in the case of sinusoidal roads. Additionally, the proposed combined controller outperforms the sky-hook controller, especially in vehicle attitude control. In detail, with an opposite-direction sinusoidal road, the control of the RMS roll angle is 9.05% higher with the proposed controller compared with the sky-hook control. For the

Table 5. List of the testing road profiles and targeted vibration modes.

Road profile	Targeted vibration mode			Description
	Vertical	Pitch	Roll	
Same-direction sinusoidal road	√			Both left and right tires encounter the same sinusoidal waves simultaneously with wave length accommodating longitudinal axis distance to allow vertical motion only. Vehicle speed is 14 km h^{-1}.
Opposite-direction sinusoidal road			√	Left and right tires experience opposite sinusoidal waves, simulating a roll motion. The vehicle speed is 10 km h^{-1}.
Torture track with square pits	√	√		Left and right tires encounter square pits at the same time or alternately, testing vehicle stability in handling potholes or sudden braking. Vehicle speed is 10 km h^{-1}.
Impact bump track	√	√	√	Left and right tires experience sudden upright bumps to simulate real-world road hazards, such as kerbs, testing vehicle stability under extreme conditions. Vehicle speed is 7 km h^{-1}.
Belgian block	√	√	√	Broadly rectangular quarried stone used in paving roads and walkways, arranged in patterns to create gaps and irregularities between the stones, testing ride comfort of the vehicle. Vehicle speed is 7 km h^{-1}.
Cobblestone	√	√	√	Highly uneven surface of large cobblestones to produce random excitation, testing ride comfort at more sparse excitation frequency. Vehicle speed is 7 km h^{-1}.

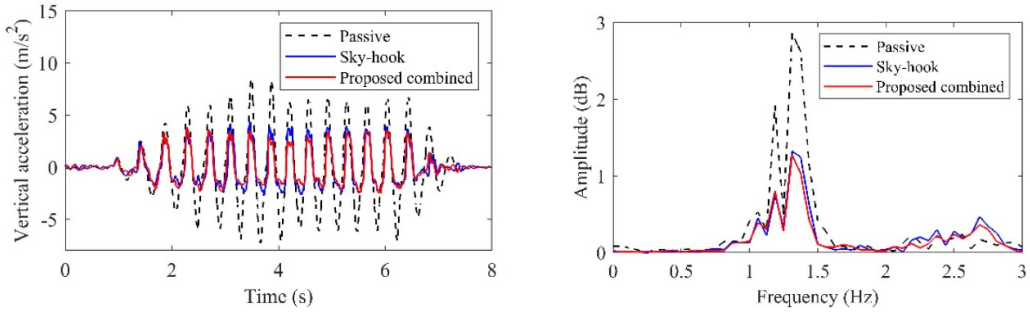

(a) (b)

Figure 19. Vertical acceleration of vehicle body under same-direction sinusoidal road: (a) time history, (b) PSD curve.

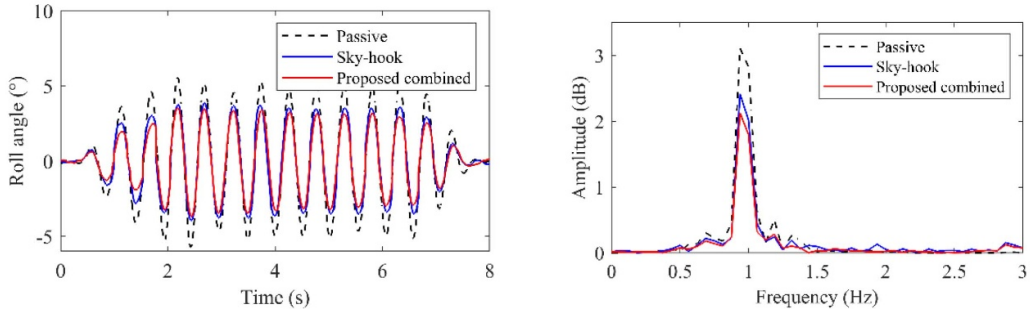

(a) (b)

Figure 20. Roll angle of vehicle body under opposite-direction sinusoidal road: (a) time history, (b) PSD curve.

Table 6. Vertical acceleration of vehicle body (m s^{-2}) on same-direction sinusoidal road.

		Semi-active suspension		Reduction ratio	
	Passive suspension	Sky-hook controller	Proposed combined controller	Sky-hook controller	Proposed combined controller
RMS	3.3075	1.6949	1.5261	48.96%	53.86%
Peak	8.4968	4.3689	3.8288	49.58%	53.94%

Table 7. Roll angle of vehicle body (deg) on opposite-direction sinusoidal road.

		Semi-active suspension		Reduction ratio	
	Passive suspension	Sky-hook controller	Proposed combined controller	Sky-hook controller	Proposed combined controller
RMS	3.0713	2.3008	2.0260	25.04%	34.09%
Peak	5.7373	3.9549	3.6705	31.07%	36.02%

the same-direction sinusoidal road, where vertical vibration is the main concern, the reduction of RMS vertical acceleration by the proposed controller is 4.9% higher than by sky-hook control.

5.3.2. Torture track with square pits. Figure 21 shows the dynamic responses of the vehicle body in the time and frequency domains under a road profile with square pits. The detailed RMS and peak values are compared in table 8.

As illustrated in figure 21, for the original vehicle, in the first two identical square pits on both sides (e.g. 0–8 s in the time domain), the vehicle body vertical acceleration and pitch angle present obvious vibration, while only a slight change in roll angle is presented. Meanwhile from 8 s to 20 s, with the alternating square pit excitation on both sides, the vehicle roll angle remarkably increases. Compared with passive suspension, both semi-active controls are able to stabilize the vehicle within the first two vibration cycles. The proposed controller and sky-hook controller achieve reductions in RMS body vertical accelerations by 37.45% and 47.65%, respectively. In terms of peak vertical acceleration, the proposed controller outperforms the sky-hook by 14.29%. For pitch and roll motion suppression, the semi-active controller demonstrates great superiority over the passive one. The proposed controller outperforms the sky-hook controller in peak pitch and roll angle reductions by 12.11% and 4.58%, respectively. The same conclusion is also presented in the PSD curve in figure 19. Near the resonant frequency of vertical motion (e.g. 1.45 Hz), compared to passive suspension, the proposed controller reduced the vehicle body vertical acceleration and pitch and roll angles by 70.93%, 64.21% and 41.49%, respectively.

5.3.3. Impact bump track. The time histories of the vehicle body vertical acceleration and pitch angle are shown in figure 22 on an impact bump track. A detailed comparison is shown in table 9. It is concluded that the proposed controller generates the best mitigation effect. Compared to passive suspension, the RMS body vertical acceleration and pitch angle with the proposed controller are reduced by 35.93% and 26.20%, respectively; the peaks of these two indices are decreased by 43.18% and 26.52%. Compared with the sky-hook controller, the proposed controller further reduces the peak body vertical acceleration and the peak pitch angle by 13.33% and 12.67%.

5.3.4. Random roads. Figure 23 shows the dynamic responses of the vehicle body in the time and frequency domains under random road profiles. Note that the road profiles are a combination of Belgian block and cobblestone tracks, with the aim of applying distinct road excitation. The detailed RMS and peak values under the random road profile are compared in table 10.

As shown in figure 23, similar to other road excitations, the proposed controller produces the best vibration mitigation. Compared to passive suspension, the RMS values of vertical acceleration, pitch and roll angle are reduced by 28.21%, 41.63% and 48.44%, while the peak values of these three indices are mitigated by 32.15%, 40.23% and 42.99% utilizing the proposed controller. In the PSD curves, the reductions in peak body vehicle acceleration and pitch and roll angle spectra by the proposed controller are 23.77%, 8.26% and 25.29%, compared with the sky-hook controller. The RMS values of these three indices are decreased by 10.41%, 18.68% and 13.65% compared with the sky-hook controller.

The above full-vehicle tests are conducted on trial repetitions, and the error bar plots of vehicle body vertical acceleration under different road profiles are shown in figure 24.

Additionally, it is experimentally demonstrated that the dynamic performance of a full vehicle with MR suspension varies under different road profile excitations. For example, the testing results show that, compared with passive suspension, the vertical acceleration RMS reduction of the vehicle

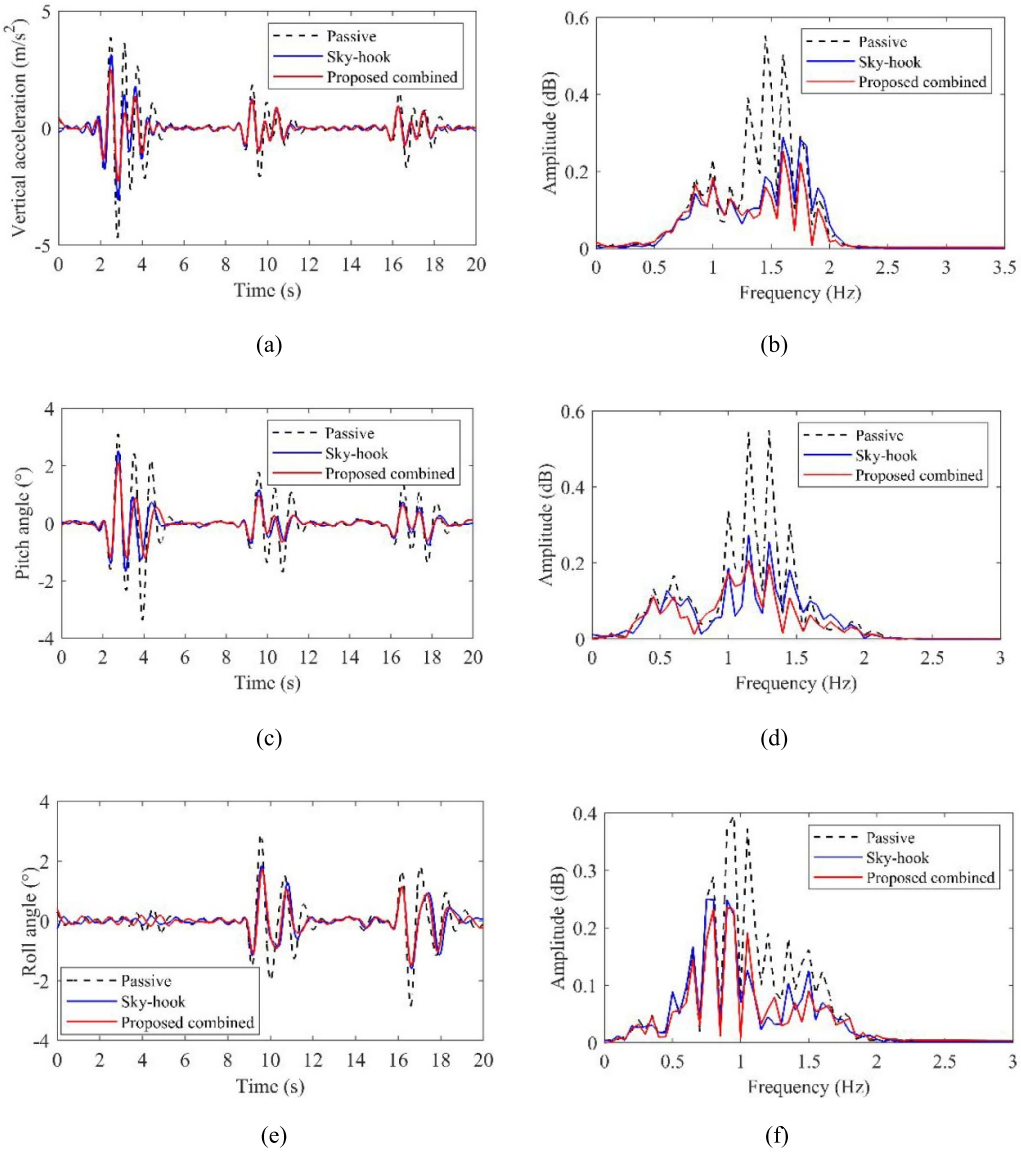

Figure 21. Dynamic responses of vehicle body on torture track with square pits: (a) time history of vertical acceleration, (b) PSD curves of vertical acceleration, (c) time history of pitch angle, (d) PSD curves of pitch angle, (e) time history of roll angle, (f) PSD curves of roll angle.

Table 8. Comparison of RMS and peak values by different controllers on torture track with square pits.

Index	Passive suspension	Semi-active suspension		Reduction ratio	
		Sky-hook controller	Proposed controller	Sky-hook controller	Proposed controller
RMS body vertical acceleration (m s^{-2})	0.8918	0.5576	0.4669	37.47%	47.65%
RMS pitch angle (deg)	0.7826	0.4428	0.3849	43.42%	50.82%
RMS roll angle (deg)	0.6591	0.4312	0.3997	34.58%	39.36%
Peak body vertical acceleration (m s^{-2})	4.6760	3.1542	2.5070	32.54%	46.38%
Peak pitch angle (deg) (m s^{-2})	3.3583	2.5350	2.1280	24.52%	36.63%
Peak roll angle (deg) (m s^{-2})	2.8935	1.8587	1.7169	36.80%	40.66%

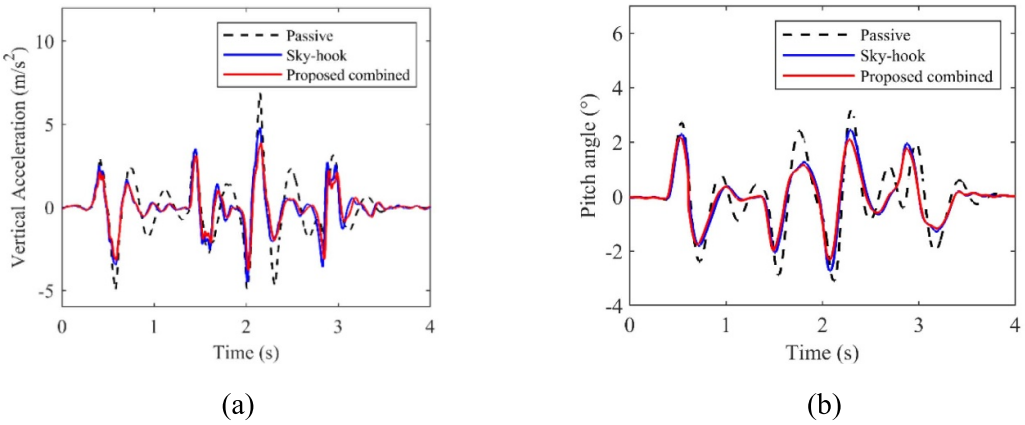

Figure 22. Dynamic responses of vehicle body on impact bump track: (a) vertical acceleration, (b) pitch angle.

Table 9. Comparison of RMS and amplitude values by different controllers under impact bump track.

Index	Passive suspension	Semi-active suspension		Reduction ratio	
		Sky-hook controller	Proposed controller	Sky-hook controller	Proposed controller
RMS body vertical acceleration (m s^{-2})	1.7179	1.2855	1.1007	25.17%	35.93%
RMS pitch angle (deg)	1.2484	1.0082	0.9213	19.24%	26.20%
Peak body vertical acceleration (m s^{-2})	6.8667	4.8167	3.9020	29.85%	43.18%
Peak pitch angle (deg) (m s^{-2})	3.1782	2.7381	2.3354	13.85%	26.52%

body on a same-direction sinusoidal road is 53.86% in table 5, which is superior to that under the random road condition (e.g. 28.2% in table 9). This is attributed to the dynamic mode response of the full-vehicle system under different road excitation characteristics. The same-direction sinusoidal excitation has typical single-frequency loading, by which only a single mode of the full vehicle is excited, while the random road excitation has broad-frequency loading, which excites multiple modes of the full vehicle. It is known that the vehicle body's vertical vibration degree under single-frequency sinusoidal road excitation is smaller than that under broad-frequency random excitations; that is, a better performance is demonstrated with a same-directional sinusoidal road (53.9%) than with a random road (28.2%).

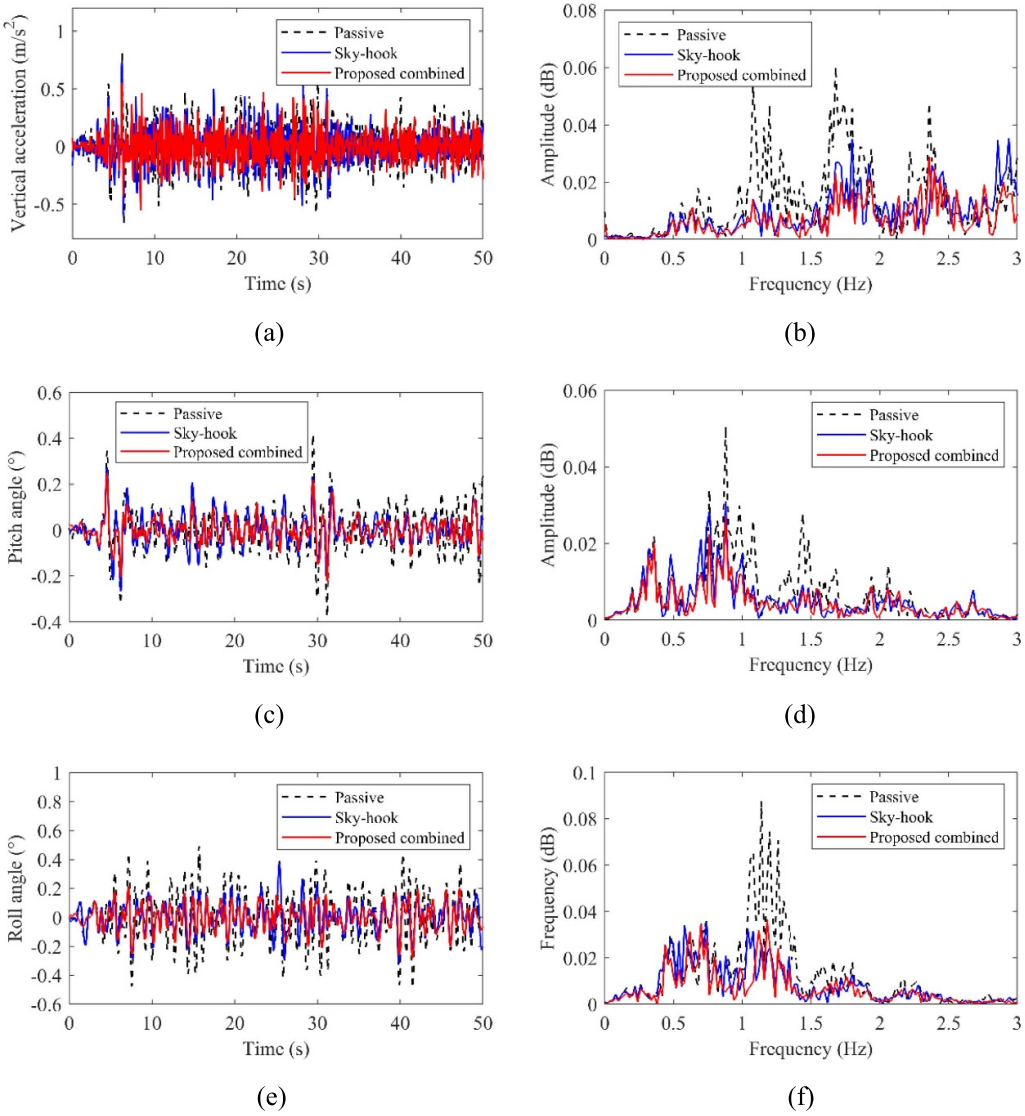

Figure 23. Dynamic responses of vehicle body under random road profiles: (a) time history of vertical acceleration, (b) PSD curves of vertical acceleration, (c) time history of pitch angle, (d) PSD curves of pitch angle, (e) time history of roll angle, (f) PSD curves of roll angle.

Table 10. Comparison of RMS and amplitude values by different controllers under random road profile.

Index	Passive suspension	Semi-active suspension		Reduction ratio	
		Sky-hook controller	Proposed controller	Sky-hook controller	Proposed controller
RMS body vertical acceleration (m s^{-2})	0.1847	0.1480	0.1326	19.87%	28.21%
RMS pitch angle (deg)	0.0932	0.0669	0.0544	28.22%	41.63%
RMS roll angle (deg)	0.1730	0.1033	0.0892	40.29%	48.44%
Peak body vertical acceleration (m s^{-2})	0.8187	0.7288	0.5555	10.98%	32.15%
Peak pitch angle (deg)	0.4181	0.2724	0.2499	34.85%	40.23%
Peak roll angle (deg)	0.4922	0.3756	0.2806	23.69%	42.99%

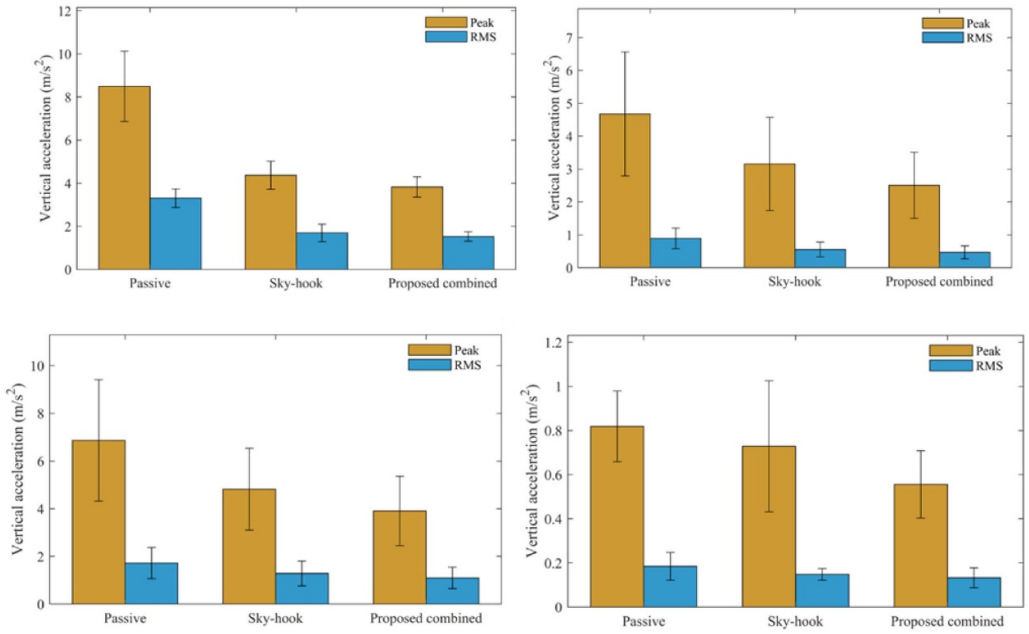

Figure 24. Error bar plots of vehicle body vertical acceleration under different road profiles: (a) same-direction sinusoidal road, (b) torture track with square pits, (c) impact bump track, (d) random road.

6. Conclusions

In this work, a novel and practical control algorithm for a full SUV with MR suspension is proposed, aiming to simultaneously control both the vehicle body's vertical vibration and its attitude motion. The dynamic characteristics of the MR damper were experimentally tested and modeled using a nonlinear Bouc—model. A quarter-vehicle setup with a double-wishbone strut and MR damper was studied, and the vertical vibration mitigation of the semi-active MR damper was experimentally validated. For full-vehicle implementation, the proposed controller is designed to control vertical vibration and maintain vehicle attitude. Unlike existing full-vehicle active controllers, this new approach directly derives the current signal, eliminating the need for complex inverse modeling of the MR damper and addressing control force tracking issues. Full-vehicle testing was conducted on various road profiles, including sinusoidal roads, torture tracks with square pits, impact bump tracks, washboards and Belgian blocks. Through experimental testing, it was demonstrated that the proposed controller not only improves ride comfort but also significantly reduces vehicle body pitch and roll.

Data availability statement

All data that support the findings of this study are included within the article (and any supplementary files).

Acknowledgment

This work was financially supported by the National Natural Science Foundation of Shandong Province (No. ZR2022ME001) and funding from Shenzhen Upward Tech Co. Ltd.

Appendix A. 7-DOF full vehicle with MR suspension

The state space equation of a 7-DOF full vehicle with MR suspension can be expressed as

$$\begin{cases} \dot{X} = AX + BU \\ Y = CX + DU. \end{cases} \tag{A-1}$$

in which X and U are respectively system state variables and input variables as follows:

$$X = \left[\begin{array}{cccccccccccccc} z_g & \theta & \phi & z_{u1} & z_{u2} & z_{u3} & z_{u4} & \dot{z}_g & \dot{\theta} & \dot{\phi} & \dot{z}_{u1} & \dot{z}_{u2} & \dot{z}_{u3} & \dot{z}_{u4} \end{array} \right]^{\mathrm{T}}$$

$$U = \left[\begin{array}{cccccccc} z_{r1} & z_{r2} & z_{r3} & z_{r4} & F_{MR1} & F_{MR2} & F_{MR3} & F_{MR4} \end{array} \right]^{\mathrm{T}},$$

in which z_g, z_{ui} and $z_{ri}\,(i = 1,2,3,4)$ are the vertical displacement of the vehicle body, the unsprung mass and the road excitation signal, respectively; θ and ϕ are the pitch angle and roll angle of the vehicle, respectively; $F_{si}(i = 1,2,3,4)$ is the spring force of suspension, which is obtained by

$$F_{si} = -k_{si}\left(z_{si} - z_{ui}\right). \tag{A-2}$$

In equation (A-1), the system matrix *A, B, C* and *D* are

$$A = \begin{bmatrix} A_1 & A_3 \\ A_2 & A_4 \end{bmatrix}$$

$$A_1 = O_{(7\times7)} \quad A_3 = E_{(7\times7)} \quad A_4 = O_{(7\times7)}$$

$$A_2 = \begin{bmatrix} a_1 & a_2 & a_3 & a_4 & a_5 & a_6 & a_7 \\ b_1 & b_2 & b_3 & b_4 & b_5 & b_6 & b_7 \\ c_1 & c_2 & c_3 & c_4 & c_5 & c_6 & c_7 \\ d_1 & d_2 & d_3 & d_4 & 0 & 0 & 0 \\ e_1 & e_2 & e_3 & 0 & e_5 & 0 & 0 \\ f_1 & f_2 & f_3 & 0 & 0 & f_6 & 0 \\ g_1 & g_2 & g_3 & 0 & 0 & 0 & g_7 \end{bmatrix}$$

$$a_1 = -(k_{s1}+k_{s2}+k_{s3}+k_{s4})/M, \quad a_2 = \left[-l_f(k_{s1}+k_{s2})+l_r(k_{s3}+k_{s4})\right]/M,$$

$$a_3 = \left[-\frac{b_f}{2}(k_{s1}-k_{s2})-\frac{b_r}{2}(k_{s3}-k_{s4})\right]/M, \quad a_4 = k_{s1}/M, \quad a_5 = k_{s2}/M, \quad a_6 = k_{s3}/M$$

$$a_7 = k_{s4}/M;$$

$$b_1 = \left[-l_f(k_{s1}+k_{s2})+l_r(k_{s3}+k_{s4})\right]/I_y, \quad b_2 = \left[-{l_f}^2(k_{s1}+k_{s2})-{l_r}^2(k_{s3}+k_{s4})\right]/I_y,$$

$$b_3 = \left[-\frac{b_f l_f}{2}(k_{s1}-k_{s2})-\frac{b_r l_r}{2}(k_{s3}-k_{s4})\right]/ I_y, \quad b_4 = l_f k_{s1}/I_y, \quad b_5 = l_f k_{s2}/I_y,$$

$$b_6 = -l_r k_{s3}/I_y \quad b_7 = -l_r k_{s4}/I_y;$$

$$c_1 = \left[-\frac{b_f}{2}(k_{s1}-k_{s2})-\frac{b_r}{2}(k_{s3}-k_{s4})\right]/ I_x, \quad c_2 = \left[-\frac{b_f l_f}{2}(k_{s1}-k_{s2})+\frac{b_r l_r}{2}(k_{s3}-k_{s4})\right]/ I_x,$$

$$c_3 = \left[-\frac{{b_f}^2}{4}(k_{s1}+k_{s2})-\frac{{b_r}^2}{4}(k_{s3}+k_{s4})\right]/ I_x, \quad c_4 = b_f k_{s1}/2I_x, \quad c_5 = b_f k_{s2}/2I_x$$

$$c_6 = b_r k_{s3}/2I_x, \quad c_7 = -b_r k_{s4}/2I_x;$$

$$d_1 = k_{s1}/m_1, \quad d_2 = k_{s1}l_f/m_1, \quad d_3 = k_{s1}b_f/2m_1, \quad d_4 = -(k_{s1}+k_t1)/m_1;$$

$$e_1 = k_{s2}/m_2, \quad e_2 = k_{s2}l_f/m_2, \quad e_3 = -k_{s2}b_f/2m_2, \quad e_5 = -(k_{s2}+k_{t2})/m_2;$$

$$f_1 = k_{s3}/m_3, \quad f_2 = -k_{s3}l_r/m_3, \quad f_3 = k_{s3}b_r/2m_3, \quad f_6 = -(k_{s3}+k_t3)/m_3;$$

$$g_1 = k_{s4}/m_4, \quad g_2 = -k_{s4}l_r/m_4, \quad g_3 = -k_{s4}b_r/2m_4, \quad g_7 = -(k_{s4}+k_{t4})/m_4$$

$$B = \begin{bmatrix} B_1 \\ B_2 \end{bmatrix} \quad B_1 = O_{(7\times8)}$$

$$B_2 = \begin{bmatrix} 0 & 0 & 0 & 0 & -1/M & -1/M & -1/M & -1/M \\ 0 & 0 & 0 & 0 & -l_f/I_y & -l_f/I_y & l_r/I_y & l_r/I_y \\ 0 & 0 & 0 & 0 & -b_f/2I_x & b_f/2I_x & -b_r/2I_x & b_r/2I_x \\ k_{t1}/m_1 & 0 & 0 & 0 & 1/m_1 & 0 & 0 & 0 \\ 0 & k_{t2}/m_2 & 0 & 0 & 0 & 1/m_2 & 0 & 0 \\ 0 & 0 & k_{t3}/m_3 & 0 & 0 & 0 & 1/m_3 & 0 \\ 0 & 0 & 0 & k_{t4}/m_4 & 0 & 0 & 0 & 1/m_4 \end{bmatrix}$$

$$C = E_{(14\times14)} \quad D = O_{(14\times8)}$$

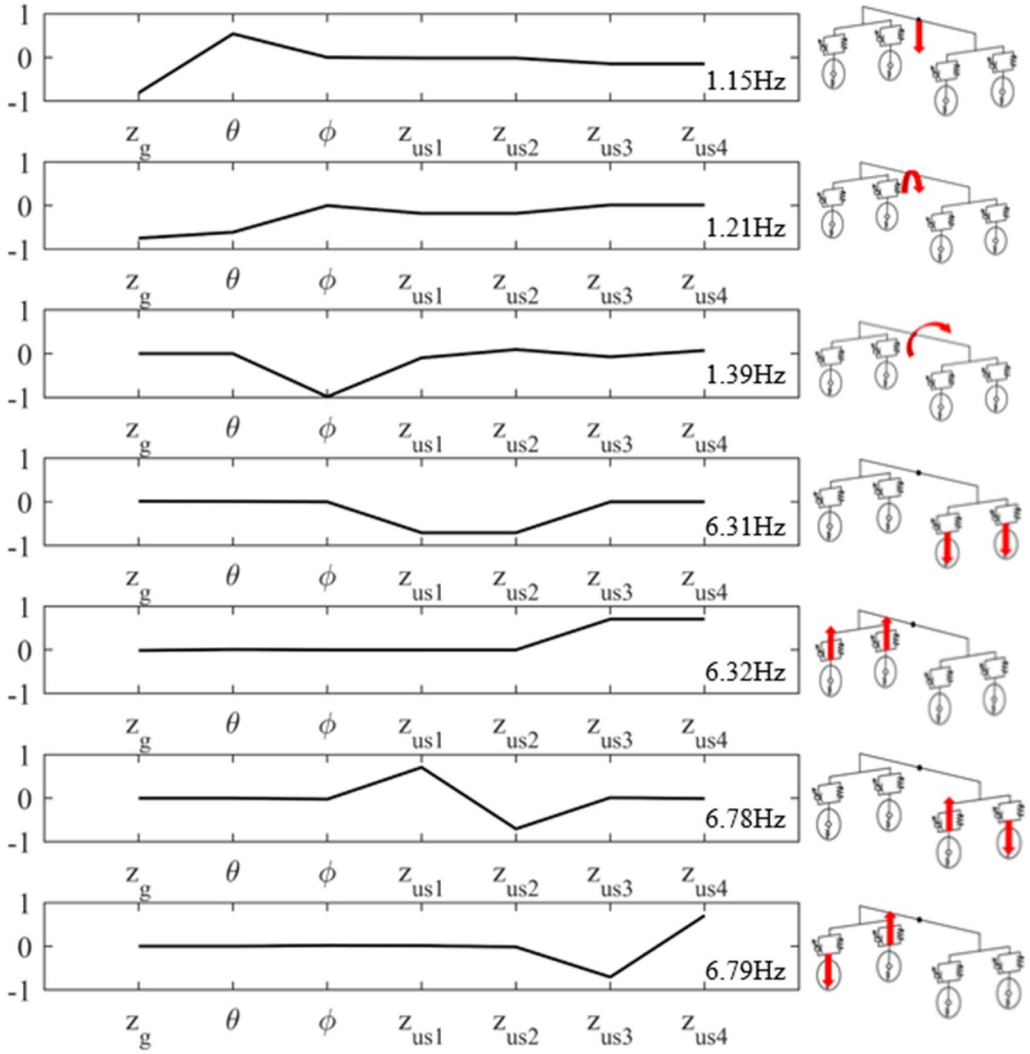

Figure A1. Vibration frequency and mode shape of full vehicle.

It is noted that $E_{(\mathrm{m}\times\mathrm{n})}$ and $O_{(\mathrm{m}\times\mathrm{n})}$ are respectively an identity matrix and a zero matrix with dimensions of $m \times n$.

In addition, the vibration frequency and mode shape are derived by the eigenvalues and eigenvectors of the dynamic model, as shown in figure A1. The sprung mass resonance focuses on the low frequency (e.g. in the range of 1–2 Hz); that is, the heave, pitch and roll resonance frequency values of the sprung mass are 1.15 Hz, 1.21 Hz and 1.39 Hz, respectively. For the unsprung mass, the resonance is in the high-frequency range (e.g. 5–7 Hz) and the main vibration mode shapes are twist and bending; that is, the resonance frequency values are 6.31 Hz, 6.32 Hz, 6.78 Hz and 6.79 Hz.

Appendix B. Quarter double-wishbone-type suspension

In geometrical analysis, the MRF damper dip angle (β) and the angles of the upper wishbone and bottom wishbone with horizontal direction (θ_1 and θ_2) are respectively derived as

$$\beta = \arctan\left(\frac{A_y - B_y}{B_z - A_z}\right) \tag{B-1}$$

$$\theta_1 = \arccos\left(\frac{N_y - M_y}{l_{\mathrm{MN}}}\right) \tag{B-2}$$

$$\theta_2 = \arccos\left(\frac{P_y - O_y}{l_{\mathrm{OP}}}\right) \tag{B-3}$$

in which $A_y, B_y, N_y, M_y, P_y, O_y$ respectively represent the instantaneous y-coordinates of the A, B, N, M, P and O points; A_z, B_z respectively represent the instantaneous z-coordinates of the A and B points; l_{MN} represents the length of the upper control arm; and l_{OP} represents the length of the lower control arm. According to the 1:1 testing platform in section 4.3, the key geometrical parameters of the quarter double-wishbone MR suspension model are derived by vision technology and listed in table B1. Based on equations (B-1)–(B-3), the MRF damper dip angle is calculated as 6.22°; the angles of the upper wishbone and bottom wishbone with horizontal direction (θ_1 and θ_2) are respectively as 5.09° and 6.10°.

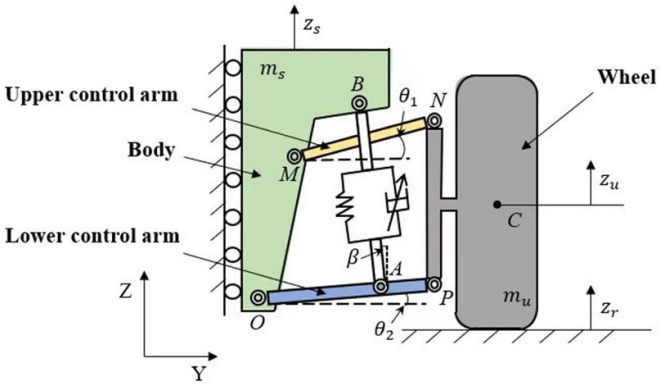

Figure B1. Quarter double-wishbone MR suspension model.

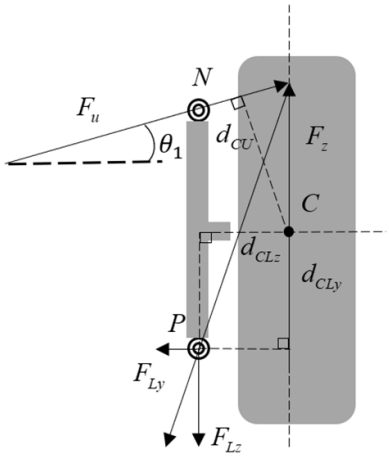

Figure B2. Force analysis of the unsprung mass in quarter suspension model.

A force analysis of individual parts (e.g. unsprung mass, bottom wishbone and sprung mass) is conducted, which derives symmetric equilibrium equations of the quarter model of SUV double-wishbone MR suspension.

Firstly, for the unsprung mass (figure B2), its equilibrium equations are expressed as

$$\begin{cases} F_z + F_{\mathrm{U}}\sin\theta_1 - F_{\mathrm{L}z} = m_{\mathrm{u}}\ddot{z}_{\mathrm{u}} \\ F_{\mathrm{U}}\cos\theta_1 - F_{\mathrm{L}y} = 0 \\ F_{\mathrm{U}}d_{\mathrm{CU}} + F_{\mathrm{L}y}d_{\mathrm{CL}y} - F_{\mathrm{L}z}d_{\mathrm{CL}z} = 0 \end{cases} \tag{B-4}$$

in which F_z represents the road force acting on the wheels, $F_z = k_{\mathrm{t}}(z_{\mathrm{r}} - z_{\mathrm{u}})$, k_{t} represents the unsprung stiffness, z_{r} represents the road excitation displacement, and z_{u} represents the vertical displacement of the wheels; F_{U} represents the force exerted on the upper control arm of the wheel; $F_{\mathrm{L}z}$ represents the force exerted on the lower control arm of the wheel in the Z direction; $F_{\mathrm{L}y}$ represents the force exerted on the lower control arm of the wheel in the Y direction; m_{u} represents the mass of the wheels; $d_{\mathrm{CL}y}$ represents the force arm from the center point C of the wheel to the force $F_{\mathrm{L}y}$, $d_{\mathrm{CL}y} = C_z - P_z$; $d_{\mathrm{CL}z}$ represents the force arm from the center point C of the wheel to the force $F_{\mathrm{L}z}$, $d_{\mathrm{CL}z} = C_y - P_y$; d_{CU} represents the force arm from the center point C of the wheel to the force F_{U}, which is

$$d_{\mathrm{CU}} = \frac{|-C_y\tan\theta_1 + M_{y0}\tan\theta_1 + C_z - M_{z0} - z_{\mathrm{s}}|}{\sqrt{1+\tan^2\theta_1}}. \tag{B-5}$$

Substituting equation (B-5) into equation (B-4),

$$\begin{cases} F_{\mathrm{U}} = \frac{d_{\mathrm{CL}z}}{d_{\mathrm{CU}} - d_{\mathrm{CL}z}\sin\theta_1 + d_{\mathrm{CL}y}\cos\theta_1}\left[k_{\mathrm{t}}(z_{\mathrm{r}} - z_{\mathrm{u}}) - m_{\mathrm{u}}\ddot{z}_{\mathrm{u}}\right] \\ F_{\mathrm{L}y} = \frac{d_{\mathrm{CL}z}\cos\theta_1}{d_{\mathrm{CU}} - d_{\mathrm{CL}z}\sin\theta_1 + d_{\mathrm{CL}y}\cos\theta_1}\left[k_{\mathrm{t}}(z_{\mathrm{r}} - z_{\mathrm{u}}) - m_{\mathrm{u}}\ddot{z}_{\mathrm{u}}\right] \\ F_{\mathrm{L}z} = \frac{d_{\mathrm{CU}} + d_{\mathrm{CL}y}\cos\theta_1}{d_{\mathrm{CU}} - d_{\mathrm{CL}z}\sin\theta_1 + d_{\mathrm{CL}y}\cos\theta_1}\left[k_{\mathrm{t}}(z_{\mathrm{r}} - z_{\mathrm{u}}) - m_{\mathrm{u}}\ddot{z}_{\mathrm{u}}\right] \end{cases} \tag{B-6}$$

Secondly, the force analysis of the bottom wishbone is shown in figure B3, and its equilibrium equations can be derived as follows:

$$\begin{cases} F_{\mathrm{O}z} = F_{\mathrm{d}}\cos\beta - F_{\mathrm{L}z} \\ F_{\mathrm{O}y} = -F_{\mathrm{L}y} - F_{\mathrm{d}}\sin\beta \\ F_{\mathrm{d}}d\beta + F_{\mathrm{L}y}d_{\mathrm{OL}y} - F_{\mathrm{L}z}d_{\mathrm{OL}z} = 0 \end{cases} \tag{B-7}$$

in which F_{d} represents the force exerted on the lower control arm by the suspension, $F_{\mathrm{d}} = [k_{\mathrm{s}}(z_{\mathrm{u}} - z_{\mathrm{s}}) - F]/\cos\beta$, k_{s} represents the suspension stiffness, z_{s} represents the vertical displacement of the vehicle body, F represents the force output by the MR damper; $F_{\mathrm{O}z}$ represents that the lower control arm is subjected to the force exerted by the vehicle body in the Z direction; $F_{\mathrm{O}y}$ represents that the lower control arm is subjected to the force exerted by the vehicle body in the Y direction;

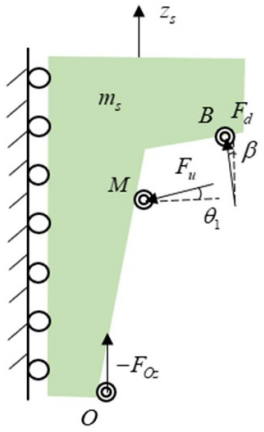

Figure B4. Force analysis of the sprung mass in quarter suspension model.

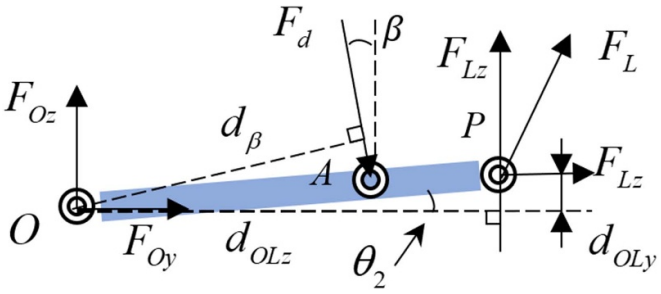

Figure B3. Force analysis of the bottom wishbone in quarter suspension model.

Table B1. Geometrical parameters of quarter double-wishbone-type suspension.

Parameter	Value (unit)	Parameter	Value (unit)
Upper control arm length, l_{MN}	0.101 m	y-coordinate of point N on the upper control arm, N_{y0}	0.136 m
Lower control arm length, l_{OA}	0.104 m	z-coordinate of point N on the upper control arm, N_{z0}	0.248 m
Lower control arm length, l_{AP}	0.082 m	y-coordinate of point P on the lower control arm, P_{y0}	0.185 m
y-coordinate of suspension point A, A_{y0}	0.103 m	z-coordinate of point P on the lower control arm, P_{z0}	0.010 m
z-coordinate of suspension point A, A_{z0}	0.011 m	Force arm d_{CU0} from point C to force, F_u	0.135 m
y-coordinate of suspension point B, B_{y0}	0.074 m	Force arm d_{CLy0} from point C to force, F_{Ly}	0.049 m
y-coordinate of suspension point B, B_{z0}	0.277 m	Force arm d_{CLz0} from point C to force, F_{Lz}	0.025 m
y-coordinate of point C at the center of the wheel, C_{y0}	0.210 m	Force arm d_{OLz0} from point O to force, F_{Lz}	0.185 m
z-coordinate of point C at the center of the wheel, C_{z0}	0.059 m	Force arm d_{OLy0} from point O to force, F_{Ly}	0.010 m
y-coordinate of point M on the upper control arm, M_{y0}	0.035 m	Force arm d_β from point O to force, F_d	0.103 m
z-coordinate of point M on the upper control arm, M_{z0}	0.239 m		

d_{OLz} represents the force arm from the origin O to the force F_{Lz}; d_{OLy} represents the force arm from the origin O to the force F_{Ly}, $d_{OLy} = l_{OP}\left|\sin\theta_2\right|$; d_β represents the force arm from the origin O to the force F_d, $d_\beta = l_{OA}\left|\sin\left(90^\circ - \theta_2 + \beta\right)\right|$.

Thirdly, the force analysis of the sprung mass is illustrated in figure B4, and its equilibrium equation is obtained as

$$-F_{Oz} + F_d\cos\beta - F_U\sin\theta_1 = m_s\ddot{z}_s \tag{B-8}$$

in which m_s represents the mass of the vehicle body.

Combining equations (B-4)–(B-8), the dynamic equation of the quarter double-wishbone-type suspension model is as follows:

$$\begin{cases} m_s\ddot{z}_s = \lambda F_d \\ m_u\ddot{z}_u = -\lambda F_d + k_t\left(z_r - z_u\right) \end{cases} \tag{B-9}$$

Appendix C. Comparison of the proposed controller and a fuzzy controller for vibration control of quarter-car model

Taking the quarter SUV model with double-wishbone MR suspension as an example, the proposed sky-hook-based vertical controller is compared with a fuzzy controller to evaluate the controllers' effectiveness. Fuzzy control rules are listed in table C1, in which z_s and z_u denote the vertical displacements of the sprung mass and unsprung mass, respectively.

Table C1. Fuzzy control rules for quarter-car model with MR suspension.

	$\dot{z}_s - \dot{z}_u$				
$\dot{z}_s$	NB	NS	Z	PB	PS
NB	H	H	M	S	S
NS	H	H	M	S	S
Z	M	M	M	M	M
PS	S	S	M	H	H
PB	S	S	M	H	H

The simulation results for sprung mass acceleration and tire dynamic loading among different controllers are shown in figure C1. It is noted that passive control denotes the MR damper at 0 A. The peak values and RMS values are compared in table C2. It is demonstrated that, in terms of sprung mass acceleration and tire dynamic loading, the present sky-hook-based controller and fuzzy controller demonstrate similar vibration mitigation effectiveness. In terms of computational efficiency, the present sky-hook-based controller only takes 9.0 s, while it takes 12.0 s for the fuzzy controller in the Simulink environment; additionally, the converted *C*-code file for HIL implementation of the present controller is 13 kB, while it is 51 kB for the fuzzy controller.

Hence, it is reasonable to apply the sky-hook-based controller, not only for its easy implementation and control effectiveness, but also for its fast solution.

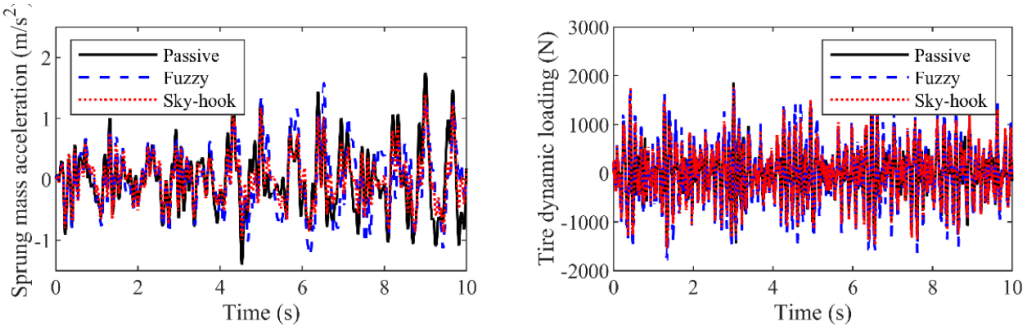

Figure C1. Numerical results of MR suspension (*B*-level road profile with driving velocity of 20 km h^{-1}): (a) sprung mass acceleration, (b) tire dynamic loading.

Table C2. Detailed comparison values of control effectiveness by different controllers.

Index	Peak values			RMS values		
	Passive	Present sky-hook-based controller	Fuzzy controller	Passive	Present sky-hook-based controller	Fuzzy controller
Sprung mass acceleration (m s^{-2})	1.7356	1.4006	1.5985	0.5216	0.3911	0.5243
Tire dynamic loading (N)	1861.6	1774.4	1922.8	493.7	535.0	626.2

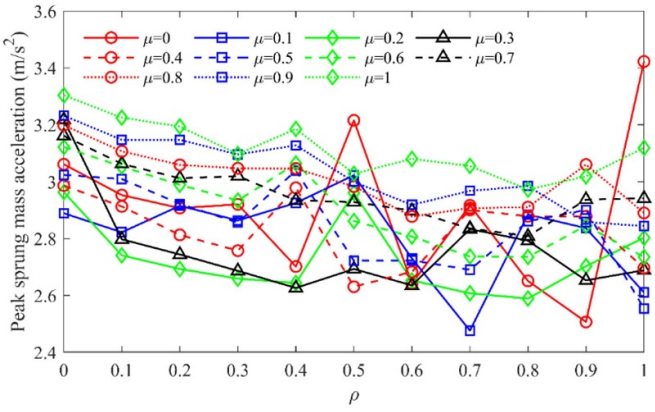

Figure D1. Peak values of sprung mass acceleration in 7-DOF full-vehicle model with different hybrid logic parameters.

Appendix D. Determination of hybrid control logic parameters (ρ and μ)

In the present work, the selection of hybrid logic control parameters is determined by the full-vehicle dynamic analysis. For generalization, a white-noise excitation whose frequency range covers 7-DOF full-vehicle modal frequencies is applied in the full-vehicle dynamic analysis. As shown in appendix A, the resonance frequencies of the studied 7-DOF SUV are focused in the range of 1.0–7.0 Hz; that is, the heave, pitch and roll modal frequencies of the sprung mass are respectively 1.15 Hz, 1.21 Hz and 1.39 Hz, and the twist and bending modal frequencies of the unsprung mass are respectively 6.31 Hz, 6.32 Hz, 6.78 Hz and 6.79 Hz. Therefore, the applied white-noise random excitation covers the frequency range 1.0 Hz–10.0 Hz. It is known that, in terms of full-vehicle vibration mitigation, the key concern is to guarantee ride comfort. Hence, the sprung mass acceleration is considered as the index, and its peak values are shown in figure D1. It is demonstrated that, when ρ and μ are respectively 0.70 and 0.10, the peak value of sprung mass acceleration achieves the minimum value. Hence, these two hybrid control logic parameters are determined and they are applied for the following full-vehicle testing.

ORCID iDs

Leng Dingxin 0000-0002-8861-2137
Zhou Xu 0009-0002-7113-9432
Liu Guijie 0000-0002-3353-117X
Li Yancheng 0000-0002-6720-8493

References

[1] Yang W, Chen J, Liu Z and Lan F 2019 Vibration characteristics of framed suv cab based on coupled transfer path analysis *Automot. Innov.* **2** 26–34
[2] Na J, Huang Y, Pei Q, Wu X, Gao G and Li G 2019 Active suspension control of full-car systems without function approximation *IEEE/ASME Trans. Mechatronics* **25** 779–91
[3] Awad S, Awad E O, Ata W G, El-Demerdash S M and Gad A S 2024 Experimental evaluation of damping and stiffness in optimized active sport utility vehicle suspension systems *Int. J. Automot. Mech. Eng* **21** 11469–85
[4] Yu M, Evangelou S A and Dini D 2021 Parallel active link suspension: full car application with frequency-dependent multiobjective control strategies *IEEE Trans. Control Syst. Technol.* **30** 2046–61

[5] Wang Z, Liu C, Zheng X, Zhao L and Qiu Y 2024 Advancements in semi-active automotive suspension systems with magnetorheological dampers: a review *Appl. Sci.* **14** 7866
[6] Li G *et al* 2024 Design and evaluation of self-tuning optimal control for vibration suppression of magnetorheological semi-active suspension *J. Low Freq. Noise Vib. Act. Control* **44** 547–64
[7] Hu T, Jiang L, Pan L Y, Chen B, Gong N, Yang J, Gong X and Sun S S 2025 Development of a semi-active suspension using a compact magnetorheological damper with negative-stiffness components *Mech. Syst. Signal Process.* **223** 111842
[8] Puneet N P, Saini R S T and Kumar H 2024 Design and fabrication of cost effective semi-active vehicular suspension system and testing on full scale quarter car suspension rig *Smart Struct. Syst.* **34** 87
[9] Kumar J and Bhushan G 2023 Dynamic analysis of quarter car model with semi-active suspension based on combination of magneto-rheological materials *Int. J. Dyn. Control* **11** 482–90
[10] Zhang H L, Cheng K Y, Wang E R, Rakheja S and Su C Y 2023 Nonlinear behaviors of a Half-car magneto-rheological suspension system under harmonic road excitation *IEEE Trans. Veh. Technol.* **72** 8592–600
[11] Jeyasenthil R, Yoon D S, Choi S B and Kim G W 2021 Robust semiactive control of a half-car vehicle suspension system with magnetorheological dampers: quantitative feedback theory approach with dynamic decoupler *Int. J. Robust Nonlinear Control* **31** 1418–35
[12] Xie L, Wang P S, Zhou W and Liao C R 2024 A simulation study on visual preview control of vehicle magnetorheological suspension *Smart Mater. Struct.* **33** 105040
[13] Zareh S H, Matbou F and Khayyat A A A 2015 Experiment of new laboratory prototyped magneto-rheological dampers on a light commercial vehicle using neuro-fuzzy algorithm *J. Vib. Control* **21** 3007–19
[14] Krauze P, Kasprzyk J and Rzepecki J 2019 Experimental attenuation and evaluation of whole body vibration for an off-road vehicle with magnetorheological dampers *J. Low Freq. Noise Vib. Act. Control* **38** 852–70
[15] Zong L H, Gong X L, Guo C Y and Xuan S H 2012 Inverse neuro-fuzzy MR damper model and its application in vibration control of vehicle suspension system *Veh. Syst. Dyn.* **50** 1025–41
[16] Du H P, Sze K Y and Lam J 2005 Semi-active H-infinity control of vehicle suspension with magneto-rheological dampers *J. Sound Vib.* **283** 981–96
[17] Wang D H and Liao W H 2005 Modeling and control of magnetorheological fluid dampers using neural networks *Smart Mater. Struct.* **14** 111–26
[18] Yan Y Y, Dong L L, Han Y and Li W S 2022 A general inverse control model of a magneto-rheological damper based on neural network *J. Vib. Control* **28** 952–63
[19] Yao J L, Taheri S, Tian S M, Zhang Z N and Shen L 2014 A novel semi-active suspension design based on decoupling skyhook control *J. Vibroengineering* **16** 1318–25
[20] Wang R C, Sheng F P, Ding R K, Meng X P and Sun Z Y 2021 Vehicle attitude compensation control of magneto-rheological semi-active suspension based on state observer *Proc. Inst. Mech. Eng. D* **235** 3299–313
[21] Wang C Y, Zhao W Z, Luan Z K, Gao Q and Deng K 2018 Decoupling control of vehicle chassis system based on neural network inverse system *Mech. Syst. Signal Process.* **106** 176–97
[22] Tang X, Du H P, Sun S S, Ning D H, Xing Z W and Li W H 2017 Takagi-sugeno fuzzy control for semi-active vehicle suspension with a magnetorheological damper and experimental validation *IEEE/ASME Trans. Mechatronics* **22** 291–300
[23] Pei P, Peng Y B and Qiu C X 2022 An improved semi-active structural control combining optimized fuzzy controller with inverse modeling technique of MR damper *Struct. Multidiscip. Optim.* **65** 272
[24] Yu M, Choi S, Dong X and Liao C 2009 Fuzzy neural network control for vehicle stability utilizing magnetorheological suspension system *J. Intell. Mater. Syst. Struct.* **20** 457–66
[25] Choi S B and Sung K G 2008 Vibration control of magnetorheological damper system subjected to parameter variations *Int. J. Veh. Des.* **46** 94–110